Gondwana Research 147 (2025) 276–300

Contents lists available at ScienceDirect

Gondwana Research

journal homepage: www.elsevier.com/locate/gr

Tectono-magmatic evolution of the Mongolian Collage with new evidence from the Ereendavaa Block

Munkhdelger Bold [a,b,*], Tatsuki Tsujimori [a], Daniel Pastor-Galán [c,d], Tatsuro Adachi [e], Nobuhiko Nakano [e], Yasuhito Osanai [e]

[a] Department of Earth Science, Graduate School of Science, Tohoku University, Sendai 980-8578, Japan
[b] Graduate School of Integrated Sciences for Global Society, Kyushu University, Fukuoka 819-0395, Japan
[c] Instituto de Geociencias (IGEO), CSIC, Madrid 28040, Spain
[d] Frontier Research Institute for Interdisciplinary Sciences, Tohoku University, Sendai 980-8576, Japan
[e] Division of Earth Sciences, Faculty of Social and Cultural Studies, Kyushu University, Fukuoka 819-0395, Japan

ARTICLE INFO

Handling Editor: Yongjiang Liu

Keywords:
Central Asian Orogenic Belt
granite
U–Pb zircon geochronology
geochemistry
microcontinent

ABSTRACT

The Central Asian Orogenic Belt, situated between the Siberian, Tarim, and North China cratons, contains three major collages, including the Mongolian Collage at its center. However, as part of the Mongolian Collage, the tectono-magmatic history of the Ereendavaa Block in northeastern Mongolia remains largely unknown. In this study, we present detailed zircon U–Pb geochronological and geochemical data from granitoids in the Ereendavaa Block, review existing data from other microcontinents within the Mongolian Collage, and integrate these findings to investigate its overall tectono-magmatic evolution. Our results reveal seven distinct magmatic episodes in the granitoids: Tonian (~880 Ma), late Ediacaran (~540 Ma), early Ordovician (~470 Ma), early Silurian (~440 Ma), late Triassic (~220 Ma), early Jurassic (~190 Ma), and middle Jurassic (~170 Ma). In addition, we identify three magmatic events from inherited zircons within the granitoids. The geochemistry of these granitoids indicates a variety of tectonic settings, predominantly forming in continental extension and arc-related environments. The spatial distribution of coeval magmatic and metamorphic events from ~880 Ma to ~440 Ma, along with older magmatic stages in microcontinents of the Mongolian Collage, suggests that the Ereendavaa Block evolved in parallel with other microcontinents within the Mongolian Collage. This evolution likely began near the Siberian Craton earlier than ~880 Ma and continued until slightly later than ~440 Ma, when the microcontinents within the Mongolian Collage may have drifted away from the Siberian Craton. Late Triassic to Middle Jurassic granitoids constrain the timing of the Mongol-Okhotsk Ocean closure in the central segment of the Mongol-Okhotsk Belt. Coeval Late Triassic formations along the southern margin of the Mongol-Okhotsk Belt support a scissor-like closure model progressing from its central to eastern segments, thereby questioning the widely accepted notion of a Triassic closure in the western segment.

1. Introduction

Microcontinents may nucleate subduction initiation at the boundary between continental and oceanic plates (e.g., Zhu et al., 2023b), potentially developing new subduction zones. Once initiated, these zones and associated processes can be recorded within the microcontinents, making them valuable archives of the surrounding tectonic evolution (e.g., Stern and Gerya, 2018). Additionally, a comprehensive understanding of the magmatic and ophiolitic complexes that have accreted to these microcontinents, along with their associated tectonic processes, is essential for elucidating key geological phenomena, including crustal growth, crustal reworking and recycling, paleogeographic reconstructions, and the long-term orogenic and geodynamic evolution (Crameri et al., 2020; Soret et al., 2022).

The Central Asian Orogenic Belt (CAOB) is one of the world's most complex preserved orogens, extending from the Siberian Craton in the north to the Tarim and North China cratons in the south (Fig. 1a). As the longest and most intricate Phanerozoic accretionary orogenic belt on Earth, the CAOB comprises a diverse array of microcontinents, ophiolites, and arc complexes, each contributing to its rich geological history

* Corresponding author at: Department of Earth Science, Tohoku University, 6-3 Aramaki Aza Aoba, Aoba-ku, Sendai, Miyagi 980-8578, Japan.
E-mail address: bold.munkhdelger.t3@dc.tohoku.ac.jp (M. Bold).

https://doi.org/10.1016/j.gr.2025.06.023
Received 9 December 2024; Received in revised form 23 June 2025; Accepted 23 June 2025
Available online 14 July 2025
1342-937X/

(e.g., Şengör et al., 1993; Windley et al., 2007; Safonova, 2017). In recent decades, there has been significant progress in understanding the existence of microcontinents and their associated magmatic and ophiolitic complexes in Mongolia, situated in the central CAOB, with studies focusing on tectonic subdivision, sedimentology, magmatism, paleomagnetism, geochronology, and geochemistry; however, the overall tectono-magmatic history of the microcontinents in Mongolia remains poorly explored (e.g., Badarch et al., 2002; Khain et al., 2003; Demoux et al., 2009a; Jian et al., 2010; Jian et al., 2014; Kröner et al., 2015; Xiao et al., 2015; Bold et al., 2016a, 2016b; Buriánek et al., 2017; Xiao et al., 2018; Bold et al., 2019; Kovach et al., 2021; Soejono et al., 2023). Two main hypotheses have been proposed regarding the origin of these microcontinents, suggesting they were derived from either the Tarim (e.g., Zhou et al., 2018) or Siberia (e.g., Collett et al., 2024) cratons.

The Ereendavaa Block (EDB), located in northeastern Mongolia, is a southeastern component of the mosaic-like structure of the Mongolian ribbon microcontinents (Fig. 1b) or Mongolian Collage microcontinents (MCMs) (e.g., Xiao et al., 2015). It is located along the southern limb of the Mongolian orocline in the central part of the CAOB and the northwestern limb of the NE China orocline in the eastern part of the CAOB (Liu et al., 2021, 2023; Zhou et al., 2025). The EDB likely preserves records of tectonic events linked to the Paleo-Asian and Mongol-Okhotsk oceans, with the closure of these oceans playing a key role in the formation of the central-eastern CAOB, as evidenced by the distribution of magmatic and metamorphic rocks of diverse ages (e.g., Miao et al., 2017, 2020).

This research aims to enhance our understanding of the tectono-magmatic evolution of the EDB, spanning from the early Neoproterozoic to the middle Jurassic, while clarifying broader tectono-magmatic relationships of the MCMs through a comprehensive examination of all relevant events in the region. For such, we have determined the timing and characteristics of the episodic magmatic events in the EDB by detailed analysis of zircon U–Pb geochronology and geochemistry for granitoids. We also thoroughly reviewed petrochronological data from the rest of the MCMs and presented an integrative view of its tectonic evolution.

2. Geological background

Reconstructing ancient paleogeography poses considerable challenges, primarily due to the significant reworking, creation, and destruction of the crust during tectonic cycles (Hoffman, 1991; Li et al., 2008; Meert and Santosh, 2017; Zhao et al., 2004, 2011, 2018). Among

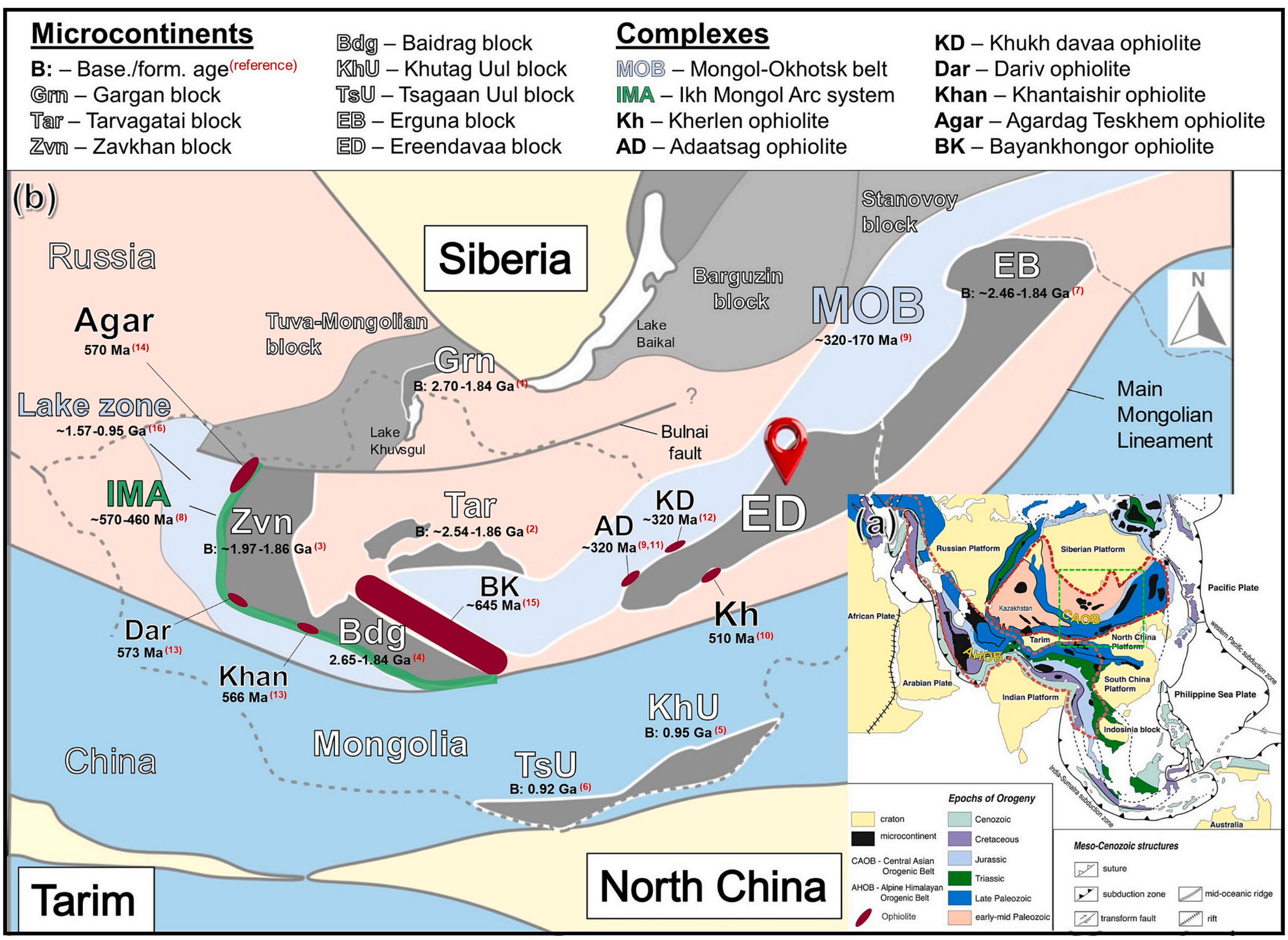

Fig. 1. (a) Tectonic map of Asia showing the locations of major cratons and orogenic belts (modified from Furnes and Safonova, 2019). (b) Approximate locations of microcontinents in the central-eastern segments of the Central Asian Orogenic Belt (modified after Şengör et al. 1993; Badarch et al., 2002; Kravchinsky et al., 2010; Ganbat et al., 2021). Representative zircon U–Pb ages for basement rocks are also displayed. References are summarized in Supplementary Table S1. The radiometric zircon ages were obtained from previously published studies: (1) Bold et al. (2019); (2) Kröner et al. (2015); (3) Bold et al. (2016a), Kovach et al. (2019); (4) Kozakov et al. (2007), Demoux et al. (2009a); (5) Yarmolyuk et al. (2005); (6) Wang et al. (2001); (7) Hou et al. (2020), Feng et al. (2022); (8) Janoušek et al. (2018), Soejono et al. (2023); (9)Tomurtogoo et al. (2005); (10) Miao et al. (2016); (11) Zhu et al. (2023a); (12) Zhu et al. (2018); (13) Jian et al. (2014); (14) Pfander et al. (2002); (15) Jian et al. (2010); (16) Buriánek et al. (2017), Skuzovatov (2021).

supercontinents, Pangea has the most reliable reconstruction, whereas Columbia's existence remains speculative (Pastor-Galán et al., 2019, 2022). Rodinia's formation and subsequent fragmentation during the Neoproterozoic are crucial for understanding Earth's paleogeographic evolution (Hoffman, 1991; Li et al., 2008; Goodge et al., 2008; Halls, 2015; Cawood et al., 2016). While its major craton configuration is partly agreed upon, the positions of smaller microcontinents remain uncertain. However, recent studies suggest the MCMs were likely along Rodinia's outer periphery (Kovach et al., 2021; Liu et al., 2020; Soejono et al., 2023).

2.1. The Central Asian Orogenic Belt

The CAOB is situated in the northern part of the Asian continent, bounded to the north by the Siberian and to the south by the Tarim-North China cratons (Fig. 1a). The tectonic evolution of the CAOB involves a complex series of subduction–accretion events, which were critical for the growth of continental crust from the Neoproterozoic through the Mesozoic, beginning with the breakup of Rodinia and followed by the opening and eventual closure of the Paleo-Asian Ocean (PAO) and Mongol-Okhotsk Ocean (MOO) (e.g., Şengör et al., 1993; Zorin, 1999; Jahn, 2004; Kröner et al., 2007; Yakubchuk, 2008; Safonova and Maruyama, 2014). The CAOB contains a wide range of geological features, including accretionary wedges, magmatic arcs, back-arc basins, ophiolites, and various microcontinents (e.g., Badarch et al., 2002; Windley et al., 2007; Xiao et al., 2015).

2.2. The Mongolian Collage

The CAOB is recognized as a super-collage formed by the amalgamation of three major collages in the Late Paleozoic: the Kazakhstan Collage in the west, the Tarim–North China Collage in the south, and the Mongolian Collage at the center–east (e.g., Xiao et al., 2015; Yakubchuk, 2008). This study primarily examines the microcontinents of Mongolia, referred to as the MCMs. Mongolian geology is divided into two tectonic domains by the Main Mongolian Lineament (Badarch et al., 2002). The northern domain is characterized by Precambrian microcontinents, Neoproterozoic to early Paleozoic subduction-accretionary complexes, metamorphic rocks, and clastic basins. In contrast, the southern domain consists mainly of middle to late Paleozoic island arc assemblages, including so-called microcontinents (Badarch et al., 2002; Windley et al., 2007).

The MCMs encompass the Gargan (a constituent of the Tuva–Mongolia Block), Tarvagatai, Zavkhan, Baidrag, and Ereendavaa (including its eastern extension, the Erguna Block in NE China) microcontinents or Blocks in the northern domain, along with the Tsagaan Uul and Khutag Uul Blocks in the southern domain (e.g., Badarch et al., 2002; Xiao et al., 2015). These microcontinents mainly consist of late Archean to Proterozoic metamorphic complexes, interspersed with Neoproterozoic to younger metasedimentary and volcanic rocks, as well as a variety of granitic intrusions of different ages (e.g., Badarch et al., 2002). Zircon U–Pb geochronology studies have confirmed the age of Precambrian basement rocks and later stages of magmatic and metamorphic events within these microcontinents. The microcontinents in the northern domain are characterized by Neoarchean to Paleoproterozoic basement rocks (~2.7–1.9 Ga), with a Paleoproterozoic magmatic/metamorphic event at ~ 1.85 Ga and a late Mesoproterozoic to early Neoproterozoic event at ~ 1 Ga, including coeval events in the Lake Zone (Fig. 1b; Khain et al., 2002; Kozakov et al., 2007; Demoux et al., 2009a, 2009b; Kröner et al., 2010; Kozakov et al., 2011; Kuzmichev and Larionov, 2013; Kröner et al., 2015; Bold et al., 2016a; Buriánek et al., 2017; Bold et al., 2019; Kovach et al., 2019; Miao et al., 2020; Skuzovatov, 2021; Feng et al., 2022). Tonian (~880–860 Ma) magmatism and high-temperature (HT) metamorphism have been recognized in the Baydrag and Zavkhan Blocks (Kozakov et al., 2012, 2014, 2017; Štípská et al., 2023). Comparable magmatic events are reported from the Gargan Block (Bold et al., 2019) and the Erguna Block (Feng et al., 2022, and references therein). In the Tarvagatai Block, these magmatic signatures are indirectly recorded through detrital zircon populations found in metapelitic rocks (Sergelen, 2018).

Several Ediacaran (~570 Ma) ophiolitic complexes bound the outer margin of the MCMs (Fig. 1b), such as Khantaishir, Dariv, and Agardag Teschem ophiolites (Pfander et al., 2002; Jian et al., 2014). In contrast, the ~ 647–636 Ma Bayankhongor ophiolite (Jian et al., 2010) is likely associated with the Ediacaran-earliest Cambrian closure of the oceanic basin between the Baydrag and Tarvagatai Blocks (e.g., Štípská et al., 2024; Sukhbaatar et al., 2024). Ediacaran–Early Cambrian magmatic complexes have been observed along the Lake Zone (Janoušek et al., 2018 and references therein). The Ordovician–Silurian one (~470–440 Ma) is also predominantly found along the MCMs (Kurimoto, 1998; Demoux et al., 2009a, 2009b; Kozakov et al., 2011; Yarmolyuk et al., 2011; Bold et al., 2016b, 2019; Feng et al., 2022). Finally, late Paleozoic–early Mesozoic magmatism is widely documented in the EDB, situated along the southern margin of the Mongol-Okhotsk Belt (MOB), unlike other MCMs (Fig. 1b; e.g., Miao et al., 2017; Ganbat et al., 2021, 2022; Zhu et al., 2023c). In addition, paleomagnetic studies indicate that the microcontinents, including the EDB, remained stable near Siberia until the late Cambrian, after which they drifted away during the Ordovician–Silurian, forming ribbon-like structures of the MCMs (Domeier and Torsvik, 2014; Kilian et al., 2016).

2.3. The Ereendavaa Block

The EDB in northeastern Mongolia constitutes an active continental margin developed through the interaction of multiple orogenic systems (Badarch et al., 2002). Two significant ophiolitic complexes mark the tectonic framework of the EDB (Fig. 2a): the Cambrian Kherlen ophiolite (~510 Ma; Miao et al., 2016) and the Carboniferous Adaatsag–Khuh Davaa ophiolites (~325 Ma; Tomurtogoo et al., 2005; Zhu et al., 2018, 2023a) are interpreted as remnants of oceanic lithosphere emplaced during subduction of the PAO (northward in present coordinates) and MOO (southward). Both are located at the western end of the EDB, with the Kherlen ophiolite along its southern margin and the Adaatsag–Khuh Davaa ophiolites along the northern margin (Fig. 1b). Thus, the EDB is a key component of the eastern CAOB, recording a complex Precambrian–Phanerozoic tectono-magmatic history. The EDB is generally characterized by Paleoproterozoic gneiss, amphibolite, schist, and marble, overlain by Neoproterozoic metasedimentary units such as black schist, metasandstone, limestone, and volcanic rocks. These units are intruded by granitic plutons of Proterozoic to younger ages (Jamyandorj et al., 1990; Badarch et al., 2002).

Pioneering efforts to reconstruct the Precambrian and Phanerozoic history of the Block, through zircon U–Pb geochronology, have been constrained by limited exposure of Precambrian strata. Only two quartzite sites (~1.2–1.1 Ga) near the Murun–Tsarigiin Gol area are currently documented (Fig. 2b; Miao et al., 2020). Previously considered basement rocks in the northeastern part of EDB, these rocks have been dated to the Phanerozoic (~490–130 Ma) (Daoudene et al., 2013; Miao et al., 2017). The Murun–Tsarigiin Gol volcanic sequence, previously thought to be Tonian to early Cambrian, is now dated to the middle Paleozoic ages (~460–416 Ma) (Fig. 2b; Narantsetseg et al., 2019). Granitoids in the Bayanmod and Murun–Tsarigiin Gol areas are dated to ~557–409 Ma (Fig. 2b; Orolmaa et al., 2015; Miao et al., 2017), while leucogranites and pegmatites in the northeastern part of EDB date to ~180–125 Ma (Daoudene et al., 2013). The tectonic evolution of the EDB's Phanerozoic history is relatively better understood than its Precambrian past (Daoudene et al., 2013; Miao et al., 2017, 2020; Narantsetseg et al., 2019, 2021).

The study area is located in the western portion of the EDB, a region of particular geological significance due to its position between ophiolitic complexes on both sides (Fig. 2a). This segment also contains a suite of granitoids exposed in a relatively underexplored zone (Fig. 2b),

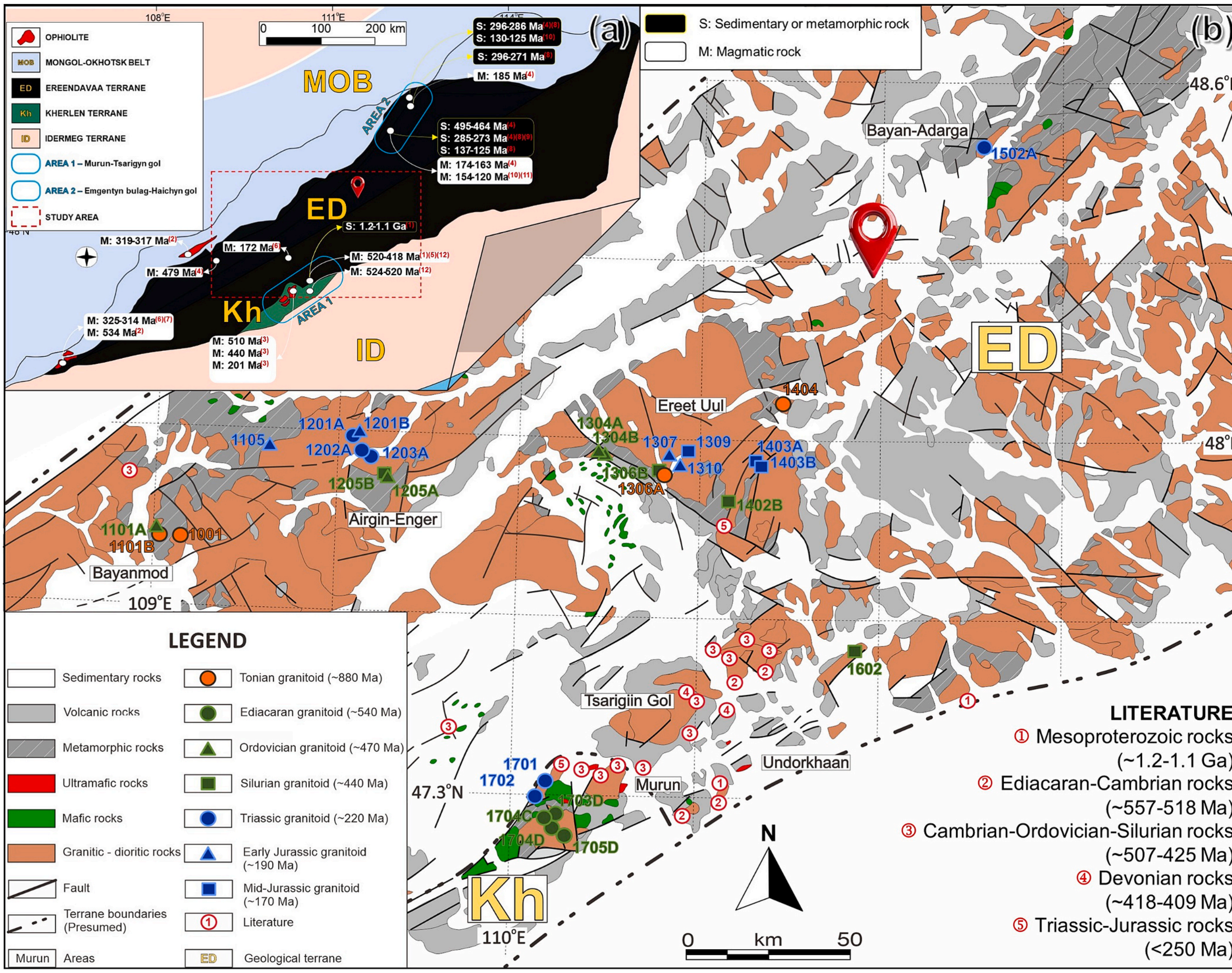

Fig. 2. (a) Location of the Ereendavaa Block with neighboring geological terranes, and the study area highlighted by the red dashed square (modified primarily from Badarch et al., 2002). Radiometric age data are sourced from: (1) Miao et al. (2020); (2) Miao et al. (2017); (3) Narantsetseg et al. (2019); (4) Narantsetseg et al. (2021); (5) Daoudene et al. (2013); (6) Daoudene et al. (2009); (7) Sheldrick et al. (2020); (8) Miao et al. (2016); (9) Tomurtogoo et al. (2005); (10) Zhu et al. (2018); (11) Zhu et al. (2023a); (12) Orolmaa et al. (2015). (b) Simplified geological map of the study area (after Jamyandorj et al., 1990), showing sample locations. The inferred boundaries of geological terranes are mostly after Badarch et al. (2002). Numbers refer to radiometric ages compiled from: (1) Miao et al. (2020); (2) Orolmaa et al. (2015); (3) Orolmaa et al. (2015), Miao et al. (2016, 2017, 2020), Narantsetseg et al. (2019); (4) Orolmaa et al. (2015), Narantsetseg et al. (2019); (5) Tomurtogoo et al. (2005).

providing critical constraints on the tectono-magmatic evolution of the Block. In several localities within the western EDB, including Bayanmod, Airgiin-Enger, Ereet Uul, Bayan-Adarga, and the western part of the Murun area (Fig. 2b), granitic intrusions display a wide range of mineral assemblages, textures, and grain sizes, reflecting the region's complex magmatic history (Jamyandorj et al., 1990). Granitic intrusions in the western EDB can be broadly categorized into seven groups based on their emplacement ages: (1) Tonian, (2) Ediacaran, (3) Ordovician, (4) Silurian, (5) Triassic, (6) Early Jurassic, and (7) Middle Jurassic (Fig. 2b).

Tonian granitoid occurs in the Bayanmod and Ereet Uul areas (Fig. 2b), typically as boulders (Fig. 3a), and is locally associated with metasedimentary rocks (Fig. 3b) or enclosed as lenses within Ordovician granitoid (Fig. 3h). Ediacaran granitoid, associated with the Kherlen Ophiolitic Complex, Kherlen terrane (Fig. 2b), forms discrete, isolated bodies with no observable contact relationships with surrounding units (Fig. 3d–e). Ordovician granitoid is exposed in the Bayanmod, Airgiin-Enger, and Ereet Uul areas (Fig. 2b), generally occurring as independent intrusive bodies (Fig. 3g), locally containing Tonian granitoid as lenses (Fig. 3h). Silurian granitoid, in the Airgiin-Enger, Ereet Uul, and Tsarigiin Gol areas (Fig. 2b), exhibits well-developed foliation (Fig. 3j) and locally intrudes metasedimentary rocks (Fig. 3k). Triassic granitoid, distributed across the Airgiin-Enger, Bayan-Adarga, and Murun areas (Fig. 2b), is characterized by a massive texture and commonly contains micrgranular mafic enclaves (MMEs; Fig. 3m). It is intruded by Early Jurassic granitoid (Fig. 3n), which displays a similarly massive fabric (Fig. 3p) and contains xenoliths of metasedimentary origin (Fig. 3q). Middle Jurassic granitoid is confined to the Ereet Uul area (Fig. 2b), and is distinguished by its K-feldspar porphyritic texture (Fig. 3s–t), with no field evidence of interaction with other rock units.

3. Analytical methods

3.1. LA–ICP–MS zircon U–Pb dating

The zircon separation and analytical procedure have been presented in detail by Kitano et al. (2014) and Adachi et al. (2012). The identification of inclusions and cathodoluminescence (CL) imaging of mounted

Fig. 3. Photographs and photomicrographs of sample outcrops in the study area. (a–c) Tonian granitoid (sample 1001); (d–f) Ediacaran granitoid (sample 1704D); (g–i) Ordovician granitoid (sample 1205A); (j–l) Silurian granitoid (sample 1205B); (m–o) Triassic granitoid (sample 1201A); (p–r) Early Jurassic granitoid (sample 1201B); (s–u) Middle Jurassic granitoid (sample 1403A). Mineral abbreviations on photomicrographs: Hbl–hornblende; Bt–biotite; Ms–muscovite; Pl–plagioclase; Kfs–K-feldspar; Qtz–quartz.

zircons were carried out using a scanning electron microprobe equipped with energy-dispersive spectroscopy (JEOL JSM-5310S-JED2140) and a CL detector (Gatan MiniCL). Zircon U–Pb dating was performed with LA–ICP–MS, employing an Agilent 7500cx quadrupole ICP–MS coupled with a New Wave Research UP-213 laser. Calibration was achieved using the Temora standard (417 Ma; Black et al., 2003), while accuracy was ensured with the FC-1 standard (1099 Ma; Paces and Miller, 1993). The NIST SRM-611 glass standard was used to determine the Th/U ratio. Concordant ages were computed using Isoplot/Ex 3.7 software (Ludwig, 2008).

3.2. Whole-rock chemistry

Major and trace elements (SiO_2, TiO_2, Al_2O_3, $Fe_2O_3^{total}$, CaO, MgO, MnO, K_2O, Na_2O, P_2O_5, V, Cr, Ni, Cu, Zn, Ga, Rb, Sr, Y, Zr, Nb, Ba) were determined on glass beads using a Rigaku Primus II X-ray fluorescence spectrometer (XRF). Detailed analytical conditions and procedures are described in Nakano et al. (2012). Glass beads were prepared by mixing the sample with lithium borate flux in a 1:2 dilution ratio using a fully automatic bead sampler (Rigaku). Rare earth elements (La, Ce, Pr, Nd, Sm, Eu, Gd, Tb, Dy, Ho, Er, Tm, Yb, Lu) and specific trace elements (Hf, Ta, Pb, Th, U) were determined by laser ablation–inductively coupled plasma–mass spectrometry (LA–ICP–MS) employing an Agilent 7500cx quadrupole ICP–MS coupled with a New Wave Research UP-213 Nd-YAG UV (213 nm) laser ablation system. These analyses were conducted directly on the glass beads used for XRF. Calibration and accuracy were verified with the NIST SRM-611 glass standard. Analytical uncertainties, which were less than 5 % of the concentration of each element, are described in the analytical procedure by Nakano et al. (2012).

3.3. Mineral chemistry

Quantitative analysis of major minerals was performed using an electron probe micro-analyzer (EPMA, JEOL JXA-8530F). The analytical conditions included an acceleration voltage of 15 kV, a beam current of 12 nA, and a beam diameter of 2 μm. Peak and background measurements were performed with varying durations: 60 s and 30 s for Cl, 90 s and 45 s for F, and 10 s and 5 s for other elements (Adachi et al., 2023). Calibration standards comprised natural and synthetic minerals and metals, with applied ZAF corrections.

All analyses, including sample preparation and petrographic observations, were conducted using the analytical facilities at Kyushu University.

4. Results

4.1. Petrography

Granitoids in the study area exhibit diverse petrographic characteristics, and predominantly have felsic compositions. The main rock types identified are granodiorite, monzogranite, syenogranite, and quartz monzodiorite. The mineral assemblage and the results of modal counting analysis are presented in Table 1, with sample coordinates provided in Supplementary Table S3. Representative outcrop photographs and thin-section photomicrographs are shown in Fig. 3.

1) Tonian granitoids (samples 1001, 1101B, 1306A, and 1404) comprise granodiorite, tonalite, and monzogranite. The modal composition includes plagioclase (36–65 vol%), K-feldspar (3–31 vol%), quartz (27–34 vol%), biotite (0.5–4 vol%), and accessory minerals (~1 vol%). Major minerals are subhedral and fine- to medium-grained, with weak to moderate foliation. Biotite commonly occurs along mineral boundaries (Fig. 3c).

2) Ediacaran granitoids (samples 1703D, 1704C, 1704D, 1705D) consist of granodiorite and monzogranite. Mineral assemblages include plagioclase (34–55 vol%), K-feldspar (17–33 vol%), quartz (19–39 vol %), hornblende (5 vol% in sample 1704D), biotite (1–10 vol%), epidote

Table 1
Mineral assemblage and modal amounts of the studied samples.

No.	Group name	Sample No.	Sample description	Pl %	Kfs	Qtz	Bt	Hbl	Ms	Ep	Opq	Acc.
1	Tonian granitoid	1001	Granodiorite	53	9	34	4				0.1	0.2
		1101B	Tonalite	65	3	30.5	0.5				0.6	0.4
		1306A	Monzogranite	36	31	30	3				0.1	0.1
		1404	Monzogranite	40	30	27	3				0.2	0.3
2	Ediacaran granitoid	1703D	Monzogranite	38	33	26	2			0.1	0.1	0.3
		1704C	Granodiorite	44	23	19	10			3.7	0.4	0.6
		1704D	Granodiorite	55	17	20	1	5		1.0	0.3	1.0
		1705D	Monzogranite	34	22	39	5			0.3	0.4	0.2
3	Ordovician granitoid	1101A	Syenogranite	21	42	23	10	1			0.8	1.5
		1205A	Granodiorite	38	20	26	11	4		0.5	0.1	0.9
		1304A	Syenogranite	14	35	48	2	1			0.4	0.4
		1304B	Syenogranite	14	27	31	27	1			0.2	0.9
4	Silurian granitoid	1205B	Granodiorite	29	31	37	2				0.1	0.1
		1306B	Monzogranite	33	37	27	3				0.2	0.5
		1402B	Monzogranite	33	33	25	8				0.2	0.1
		1602	Monzogranite	27	23	49	1				0.3	0.2
5	Triassic granitoid	1201A	Tonalite	53	3	18	15	11			0.1	0.3
		1202A	Quartzdiorite	62	2	6	18	12		0.1	0.4	0.2
		1203A	Quartzmonzodiorite	53	9	12	13	12		0.4	0.1	0.6
		1502A	Granodiorite	49	8	22	10	7		2.4	0.5	1.1
		1701	Granodiorite	44	21	29	5			0.1	0.3	0.3
		1702	Granodiorite	50	19	23	8			0.1	0.2	0.3
6	Early Jurassic granitoid	1105	Monzogranite	26	44	29	1		0.3		0.2	0.4
		1201B	Monzogranite	39	28	29	3		1.0		0.1	0.7
		1307	Monzogranite	25	38	26	10		1.0	0.4	0.3	0.4
		1310	Monzogranite	32	27	37	3		0.8		0.2	0.3
7	Mid–Jurassic granitoid	1309	Syenogranite	25	46	21	7			0.2	0.3	0.7
		1403A	Quartz monzodiorite	49	21	14	15				0.3	0.9
		1403B	Monzogranite	39	25	28	8				0.3	0.5

Note: Sample descriptions based on the QAP diagram.
Abbreviation: Pl – plagioclase, Kfs – K-feldspar, Qtz – quartz, Bt – biotite, Amp – amphibole, Ms – muscovite, Ep – epidote, Opq – opaque mineral, and Acc. – accessory mineral.

(0.1–3.7 vol%), and accessory minerals (~1 vol%). Minerals are fine to medium-grained, primarily subhedral in shape (Fig. 3f).

3) Ordovician granitoids (samples 1101A, 1205A, 1304A, and 1304B) include granodiorite and syenogranite, with plagioclase (14–38 vol%), K-feldspar (20–42 vol%), quartz (23–48 vol%), hornblende (1–4 vol%), biotite (2–27 vol%), and accessory minerals (~1 vol%). Major minerals are moderately oriented and vary from fine- to coarse-grained (Fig. 3i).

4) Silurian granitoids (samples 1205B, 1306B, 1402B, and 1602) consist of granodiorite and monzogranite. Mineral compositions include plagioclase (27–33 vol%), K-feldspar (23–37 vol%), quartz (25–49 vol %), biotite (1–8 vol%), and accessory minerals (~1 vol%). Major minerals are strongly oriented, with grain sizes ranging from fine to medium (Fig. 3l).

5) Triassic granitoids (samples 1201A, 1202A, 1203A, 1502A, 1701, and 1702) include quartz diorite and granodiorite, with plagioclase (44–62 vol%), K-feldspar (2–21 vol%), quartz (6–29 vol%), hornblende (7–12 vol%, excluding samples 1701 and 1702), biotite (5–18 vol %), epidote (0.1–2.4 vol%), and accessory minerals (~1 vol%). Magmatic epidote is common, and sample 1502A notably contains euhedral and medium-grained titanite (Fig. 3o).

6) Early Jurassic granitoids (samples 1105, 1201B, 1307, and 1310) consist of monzogranite with plagioclase (25–39 vol%), K-feldspar (27–44 vol%), quartz (26–37 vol%), biotite (1–10 vol%), muscovite (0.3–1.0 vol%), and accessory minerals (~1 vol%). Major minerals are typically subhedral to euhedral (Fig. 3r).

7) Mid–Jurassic granitoids (samples 1309, 1403A, and 1403B) comprise syenogranite, quartz monzodiorite, and monzogranite, with plagioclase (25–49 vol%), K-feldspar (21–46 vol%), quartz (14–28 vol %), biotite (7–15 vol%), and accessory minerals (~1 vol%). Compared to other granitoid types, the mineral grains are notably coarser (Fig. 3u).

4.2. U–Pb zircon geochronology

Sixteen samples from the study area were dated using LA–ICP–MS, summarized in Table 2, with detailed data in Supplementary Table S4. At least two representative samples from each granitoid type were selected for zircon U–Pb dating. Representative CL images of zircon, Th/U ratios, and Concordia diagrams are shown in Fig. 4. Zircons typically exhibit well-developed oscillatory zoning, with rare sector zoning, as observed in the CL images (Fig. 4a). Zircon shapes vary from stubby to elongated prisms, with grain sizes ranging from approximately 50 to 500 µm, containing inclusions of plagioclase, apatite, and quartz. Zircons from Tonian (samples 1001 and 1101B) and Ediacaran granitoids (samples 1704D and 1703D) are predominantly rounded, with occasional overgrowth textures. Analyses were conducted on inclusion-free and crack-free zircon portions (Fig. 4a). Their Th/U ratios are generally greater than 0.1 (Fig. 4b). The Concordia ages, derived from concordant data, and the mean ages, based on ^{206}Pb/^{238}U ratios, are both interpreted as the crystallization ages of the granitoids (Table 2).

Tonian granitoids. Sample 1001: Twenty-four concordant and seven discordant data points were obtained from thirty-one analyses. Inherited zircons showed older dates of 963 and 1011 Ma (Th/U = 0.265 and 0.215). The remaining twenty-one concordant data points, with Th/U ratios from 0.208 to 0.384, provided a Concordia age of 880.2 ± 6.5 Ma (Fig. 4c). A zircon with an overgrowth rim yielded a younger concordant datum of 444 Ma (Th/U = 0.022). Sample 1101B: Twenty-three concordant and seven discordant data points were obtained. The youngest date population (10 concordant data points, Th/U = 0.068–0.181) yielded a Concordia age of 881.9 ± 12 Ma (Fig. 4c). Inherited dates from 932 to 1346 Ma (Th/U = 0.067–0.458) were also detected.

Ediacaran granitoids. Sample 1704D: Twenty-three analyses yielded Th/U ratios between 0.207 and 1.196, with ^{206}Pb/^{238}U dates ranging from 528 to 599 Ma. The youngest date population (16 concordant data points) produced a Concordia age of 544.7 ± 4.9 Ma. An overgrowth rim yielded a younger date of 451 Ma (Th/U = 0.663) (Fig. 4d). Sample 1703D: Sixteen analyses, with Th/U ratios from 0.145 to 0.915 and ^{206}Pb/^{238}U dates from 525 to 579 Ma, yielded a weighted mean age of 542.1 ± 8.6 Ma (Fig. 4d).

Ordovician granitoids. Sample 1205A: Thirteen concordant and one discordant data points, with Th/U ratios from 0.336 to 0.855, yielded a concordia age of 470.8 ± 4.7 Ma from twelve concordant data points (Fig. 4e). Sample 1101A: Fourteen concordant and four discordant data points, with Th/U ratios from 0.479 to 0.915, provided a Concordia age of 472.9 ± 5.2 Ma (n = 11, MSWD = 0.03) (Fig. 4e).

Silurian granitoids. Sample 1205B: Nineteen concordant and four discordant data points, with Th/U ratios from 0.272 to 1.322 and ^{206}Pb/^{238}U ages from 420 to 454 Ma, yielded a concordia age of 437.9 ± 3.5 Ma (Fig. 4f). Sample 1602: Fifteen concordant and nine discordant data points, with Th/U ratios from 0.465 to 0.767, yielded a Concordia age of 431.4 ± 3.6 Ma (n = 14, MSWD = 0.12) (Fig. 4f).

Triassic granitoids. Four samples (1201A, 1203A, 1502A, and 1701) yielded Concordia ages ranging from 207.8 ± 2.6 Ma to 226.1 ± 3.1 Ma (Fig. 4g–h; Table 2). Sample 1201A: Fifteen analyses yielded concordant data, with Th/U ratios from 0.590 to 1.597, resulting in a Concordia age of 207.8 ± 2.6 Ma (n = 15, MSWD = 0.011). Sample 1203A: Fourteen analyses yielded Th/U ratios from 0.514 to 1.493, with

Table 2
Summary of the zircon U–Pb ages of the dated samples.

Sample description	Sample No.	Th/U ratio	n^t	n^c	MSWD	Concordia age, Ma	Inherited dates, Ma (n)	Overgrowth dates, Ma (n)
Tonian granitoid	1001	0.02–0.48	31	21	0.01	880.2 ± 6.5	750–761(2), 844(1), 879–1068(6)	444(1)
	1101B	0.07–0.63	30	10	0.21	881.9 ± 12	724 (1), 931–1354 (19)	–
Ediacaran granitoid	1703D	0.14–0.92	16	16	2.50	*542.1 ± 8.6	–	–
	1704D	0.21–1.19	23	16	0.17	544.7 ± 4.9	565–599(6)	451(1)
Ordovician granitoid	1101A	0.48–0.92	16	11	0.03	472.9 ± 5.2	500 (1)	–
	1205A	0.33–0.85	14	12	0.09	470.8 ± 4.7	509 (1)	–
Silurian granitoid	1205B	0.27–3.92	23	19	0.26	437.9 ± 3.5	–	–
	1602	0.39–1.34	24	14	0.12	431.4 ± 3.6	475(1), 600(1)	–
Triassic granitoid	1201A	0.59–1.60	15	15	0.01	207.8 ± 2.6	–	–
	1203A	0.51–1.49	14	14	0.43	218.8 ± 2.8	–	–
	1502A	0.10–2.71	28	18	0.81	*214.7 ± 5.3	294(1), 425–436(3), 812–881(5)	–
	1701	0.06–1.62	15	8	0.68	226.1 ± 3.1	257–297(3), 424(3), 532–559(2), 827(1)	–
Early Jurassic granitoid	1307	0.07–1.04	38	30	5.80	*183.6 ± 5.9	242–308(5), 410(1), 565(1), 639(1)	–
	1201B	0.44–2.26	24	18	0.11	192.8 ± 2.4	221–239(2), 461–462(2)	–
Mid–Jurassic granitoid	1309	0.06–2.02	18	16	1.80	*173.5 ± 4.9	210(1), 291(1)	–
	1403A	0.16–0.93	14	14	2.50	171.5 ± 2.2	–	–

n^t – the total number of analyses.
n^c – number of data used for calculating Concordia/Mean age.
n – number of inherited zircon and core-overgrowth dates.
* – weighted mean age.

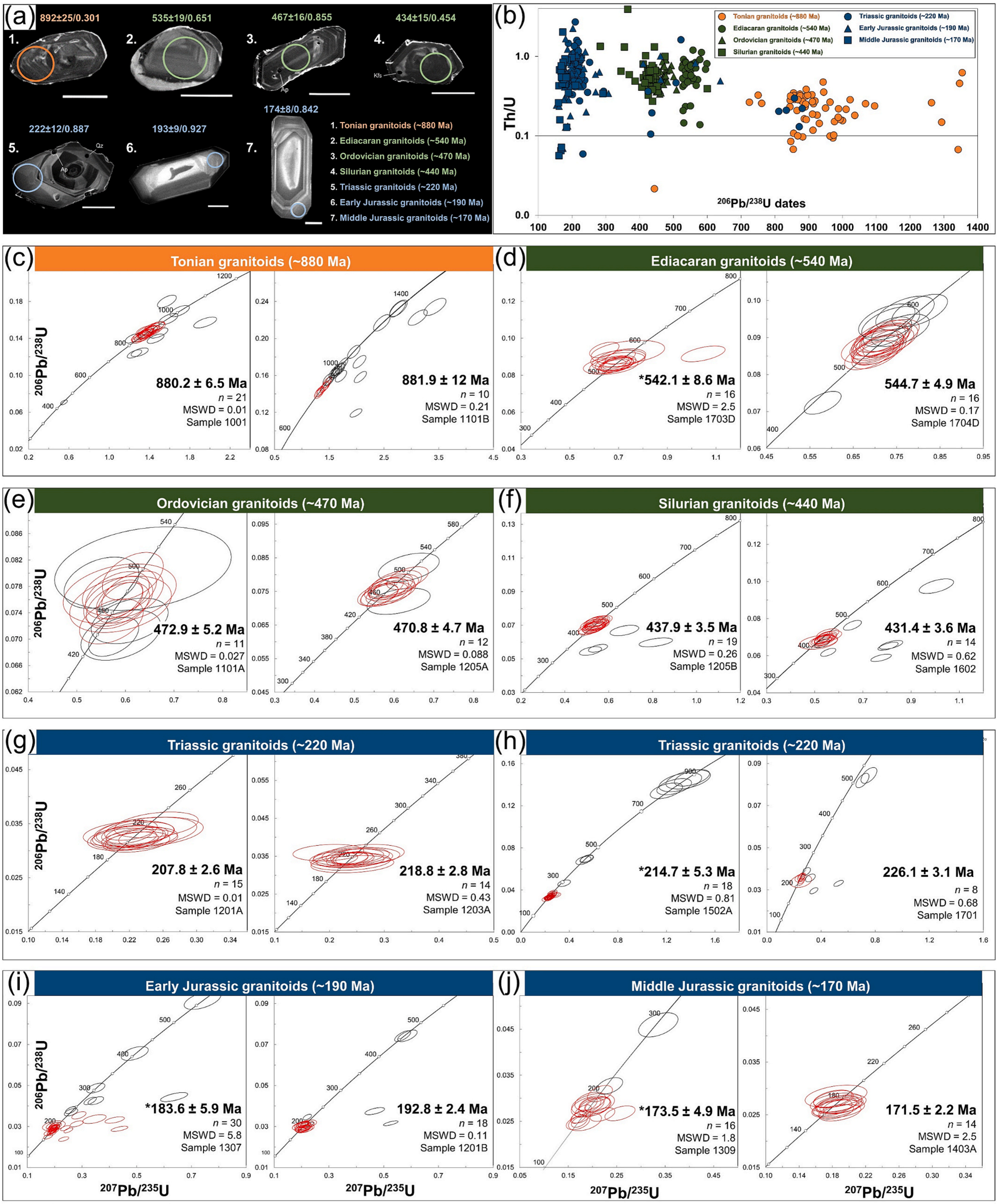

*Note: * indicates the weighted mean age.*

Fig. 4. (a) Cathodoluminescence images of representative zircons from dated samples. $^{206}Pb/^{238}U$ age, with 2σ error and the Th/U ratio. Analysis spots are marked by colored circles, and scale bars (50 μm) are included. Abbreviations for zircon inclusions: Ap–apatite; Kfs–K-feldspar; Qz–quartz. (b) $^{206}Pb/^{238}U$ age (Ma) versus Th/U ratio for zircons from dated samples. (c) Concordia diagrams for zircon U–Pb dating, showing the Concordia/weighted mean age, mean square weighted deviation (MSWD), number of analyses (*n*) used for age calculation, and sample number. Red ellipsoids represent analyses included in the age calculation, whereas grey ellipsoids mark those excluded.

$^{206}Pb/^{238}U$ dates from 209 to 228 Ma, resulting in a concordia age of 218.8 ± 2.8 Ma. Sample 1502A: Twenty-four concordant and four discordant data points, with $^{206}Pb/^{238}U$ dates from 201 to 881 Ma, produced a weighted mean age of 214.7 ± 5.3 Ma (n = 18, MSWD = 0.81). Sample 1701: Eight concordant and seven discordant data points, with Th/U ratios from 0.059 to 0.641, yielded a Concordia age of 226.1 ± 3.1 Ma (n = 8, MSWD = 0.68).

Early Jurassic granitoids. Sample 1201B: Twenty-four analyses yielded twenty concordant and four discordant data points. The predominant group of nineteen concordant data points, with Th/U ratios from 0.511 to 1.670, provided a Concordia age of 192.8 ± 2.4 Ma (Fig. 4i). Inherited zircons were identified, with dates from 220 Ma to 462 Ma. Sample 1307: Thirty-eight analyses yielded twenty-four concordant and fourteen discordant data points. Th/U ratios ranged from 0.070 to 1.041, with $^{206}Pb/^{238}U$ dates from 154 to 235 Ma, resulting in a weighted mean age of 183.6 ± 5.9 Ma (n = 30, MSWD = 5.80). Inherited zircons were also identified, with dates from 242 to 639 Ma (Fig. 4i).

Mid–Jurassic granitoids. Sample 1403A: Fourteen concordant data points, with Th/U ratios from 0.159 to 0.930, yielded a Concordia age of 171.5 ± 2.2 Ma (Fig. 4j). Sample 1309: Eighteen analyses of fourteen zircons, with two grains yielding inherited dates of 291 and 210 Ma (Th/U = 0.340 and 0.431), yielded a weighted mean age of 173.5 ± 4.9 Ma (n = 16, MSWD = 1.80) (Fig. 4j).

4.3. Whole-rock geochemistry

Twenty-nine samples spanning from the Tonian (~880 Ma) to the middle Jurassic (~170 Ma) were subjected to whole-rock geochemical analysis. The major and trace element geochemical data are presented in Supplementary Table S5.

Tonian granitoids (~880 Ma). The granitoids exhibit a granitic composition (Fig. 5a), fitting within the calc-alkaline to high-K calc-alkaline series (Fig. 5b) and showing a ferroan signature (Fig. 5c). They are peraluminous, with aluminum saturation index (ASI) values from 1.05 to 1.26 (Fig. 5d). Their major element compositions are characterized by SiO_2 ranging from 70.6 to 75.8 wt%, total alkalis from 6.60 to 8.95 wt%, Al_2O_3 from 13.7 to 16.8 wt%, TiO_2 from 0.10 to 0.29 wt%, and CaO from 0.65 to 2.40 wt%. MgO varies from 0.14 to 0.50 wt%, and FeO^T from 0.37 to 1.17 wt%, with Mg# values ranging from 29.5 to 52.3. Rare earth element (REE) patterns are characterized by light REE (LREE) enrichment and flat heavy REE (HREE) [$(La/Yb)_N$ = 7.69–22.9], with variable Eu anomalies: strongly negative (Eu/Eu* = 0.21) for sample 1101B and weakly positive (Eu/Eu*=0.86–1.70) for others (Fig. 6a). Multi-element patterns show negative Nb, P, and Ti anomalies, with significant Rb, K, and Pb enrichment (Fig. 6b).

Ediacaran granitoids (~540 Ma). These granitoids, including granodiorite and granite (Fig. 5a), have SiO_2 values ranging from 68.9 to 76.0 wt%, total alkalis from 6.49 to 9.19 wt%, Al_2O_3 from 11.9 to 15.4 wt%, TiO_2 from 0.18 to 0.40 wt%, and CaO from 0.18 to 3.77 wt%. MgO ranges from 0.16 to 0.69 wt%, and FeO^T from 1.14 to 2.35 wt%, with Mg# values from 18.6 to 38.7. They are classified within the calc-alkaline to high-K calc-alkaline series (Fig. 5b), ferroan (Fig. 5c), and display metaluminous to weakly peraluminous characteristics, with ASI values of 0.93–1.11 (Fig. 5d). REE patterns show LREE enrichment and flat HREE [$(La/Yb)_N$ = 2.39–4.51] with negative Eu anomalies (Eu/Eu* = 0.35–0.74) (Fig. 6c). Multi-element patterns indicate significant enrichment in K and Pb and slight to moderate depletion in Nb, P, and Ti (Fig. 6d).

Ordovician granitoids (~470 Ma). These granitoids have higher silica content, with SiO_2 ranging from 72.1 to 81.9 wt%, total alkalis from 5.48 to 8.46 wt%, Al_2O_3 from 9.62 to 14.6 wt%, TiO_2 from 0.20 to 0.35 wt%, and CaO from 0.05 to 1.74 wt%. MgO varies from 0.30 to 0.52 wt%, and FeO^T from 1.0 to 2.63 wt%, resulting in Mg# values from 18.6 to 43.6. They belong to the high-K calc-alkaline series (Fig. 5b), are ferroan (Fig. 5c), and exhibit various ASI values from 1.02 to 1.42

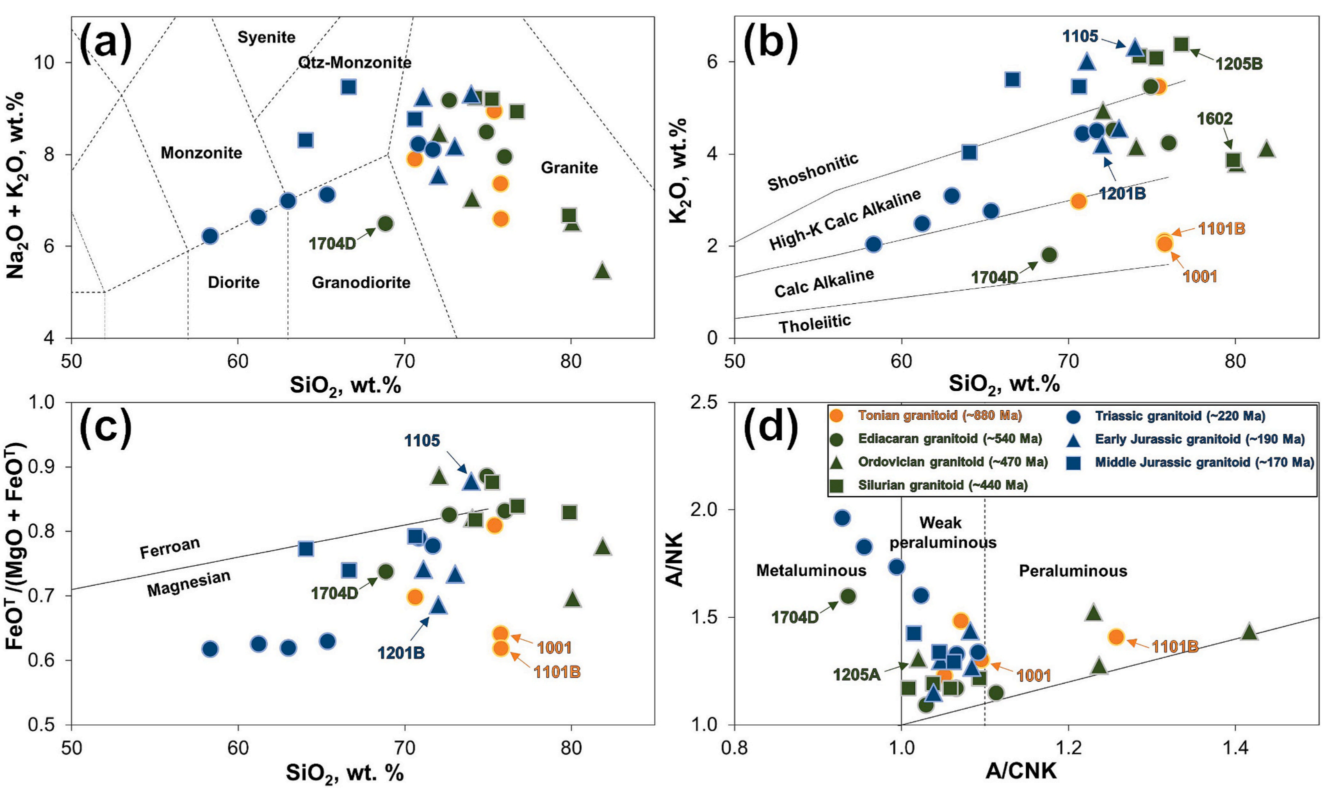

Fig. 5. (a) $Na_2O + K_2O$ versus SiO_2 (TAS) diagram for plutonic rocks (after Middlemost, 1994); (b) K_2O versus SiO_2 diagram for subdivision of sub-alkalic rocks (after Peccerillo and Taylor, 1976); (c) FeO^T / ($MgO + FeO^T$) versus SiO_2 plot for magnesian and ferroan rocks (after Frost et al., 2001); (d) A/NK [molar $Al_2O_3/(Na_2O + K_2O)$] versus A/CNK [molar $Al_2O_3/(CaO + Na_2O + K_2O)$] diagram (after Maniar and Piccoli, 1989).

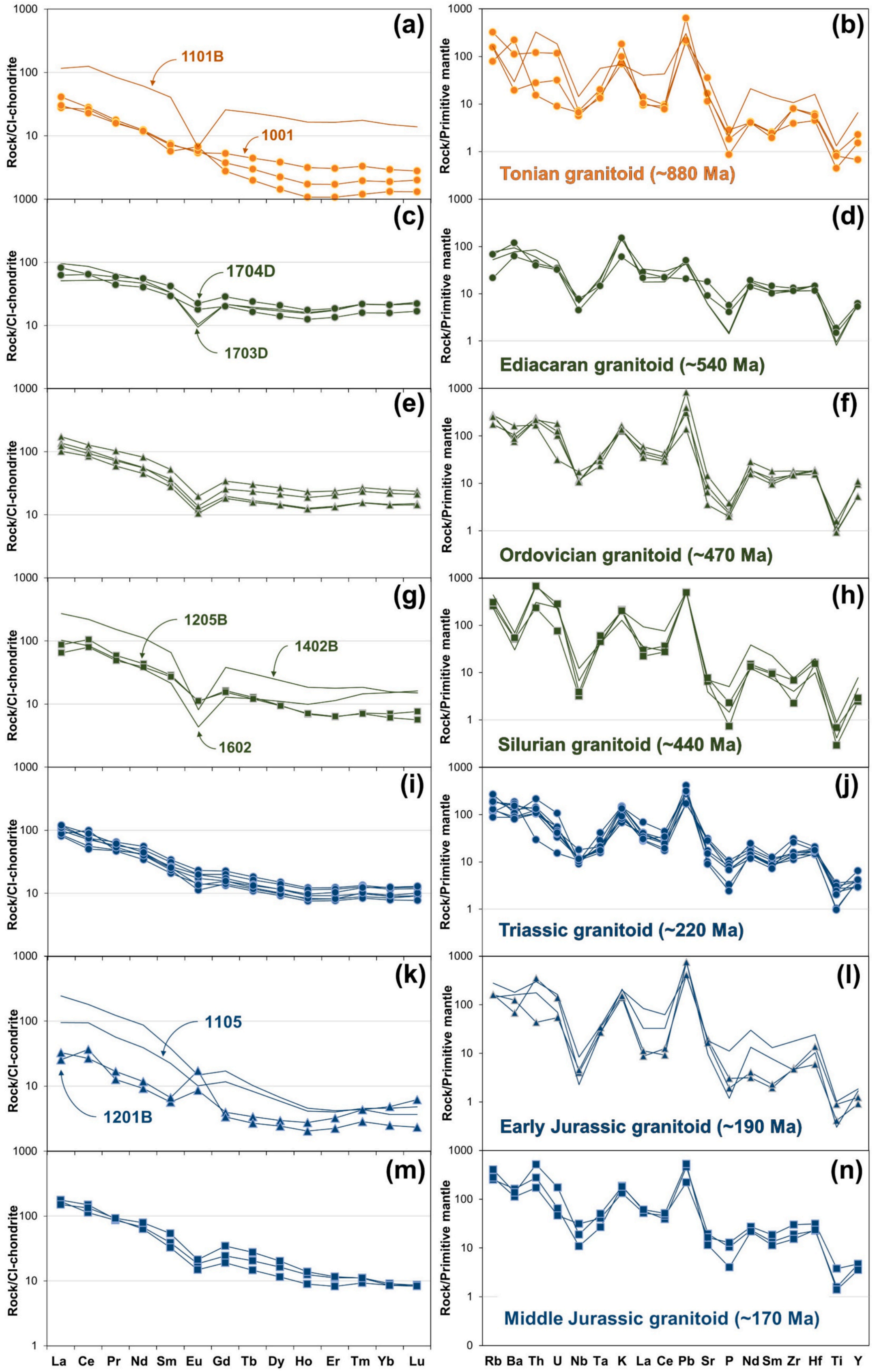

Fig. 6. CI-chondrite-normalized REE patterns and primitive-mantle-normalized multi-element patterns (spider diagram) for the studied samples. Normalizing values from Sun & McDonough (1989).

(Fig. 5d). REE patterns are marked by LREE enrichment and flat HREE [$(La/Yb)_N$ = 5.65–9.40] with negative Eu anomalies (Eu/Eu* = 0.45–0.48) (Fig. 6e). Primitive mantle-normalized trace element patterns show enrichment in Rb, K, and Pb and depletion in Nb, Sr, P, and Ti (Fig. 6f).

Silurian granitoids (~440 Ma). These granitoids feature higher SiO_2 values from 74.2 to 79.9 wt%, total alkalis from 6.68 to 9.23 wt%, and Al_2O_3 from 10.3 to 14.3 wt%, with lower TiO_2 (0.06–0.19 wt%) and FeO^T (0.61–1.27 wt%) and moderate Mg# (20.1–28.4). They are classified as high-K calc-alkaline to shoshonitic (Fig. 5b), magnesian (Fig. 5c), and weakly peraluminous with ASI of 1.01–1.09 (Fig. 5d). REE patterns show two distinct types: low LREE/HREE ratios [$(La/Yb)_N$ = 10.7–12.5] with weak negative Eu anomalies (Eu/Eu* = 0.51–0.55), and high LREE/HREE ratios [$(La/Yb)_N$ = 6.76–17.3] with strong negative Eu anomalies (Eu/Eu* = 0.16–0.26) (Fig. 6g). Multi-element patterns reveal negative anomalies in Ba, Nb, Sr, P, and Ti, with substantial enrichment in Rb, Th, K, and Pb (Fig. 6h).

Triassic granitoids (~220 Ma). Hbl–Bt granitoids range from diorites to granites, with SiO_2 values between 58.3 and 71.7 wt%, total alkalis from 6.22 to 8.23 wt%, Al_2O_3 from 14.5 to 17.8 wt%, and TiO_2 from 0.21 to 0.78 wt%. MgO ranges from 0.42 to 3.43 wt%, and FeO^T from 1.50 to 5.53 wt%, giving Mg# values from 32.1 to 52.4. They belong to the high-K calc-alkaline series (Fig. 5b), are magnesian (Fig. 5c), and show metaluminous to weakly peraluminous characteristics with ASI values from 0.93 to 1.09 (Fig. 5d). REE patterns indicate moderate LREE enrichment [$(La/Yb)_N$ = 8.50–11.7] with weakly negative Eu anomalies (Eu/Eu* = 0.62–0.93) (Fig. 6i). Multi-element patterns display enrichment in Rb, K, and Pb, with pronounced negative anomalies in Nb, P, and Ti (Fig. 6j).

Early Jurassic granitoids (~190 Ma). Two mica granitoids exhibit SiO_2 values from 71.1 to 74.0 wt%, total alkalis from 7.55 to 9.32 wt%, and Al_2O_3 from 13.5 to 15.0 wt%, with lower TiO_2 (0.07–0.22 wt%), MgO (0.11–0.68 wt%), and FeO^T (0.51–1.49 wt%), and moderate Mg# (19.8–44.9). They are classified as granite (Fig. 5a) and belong to the high-K calc-alkaline to shoshonitic series (Fig. 5b), with a magnesian type (Fig. 5c) and weakly peraluminous traits with ASI values of 1.01–1.09 (Fig. 5d). Their REE patterns reveal two distinctive features: slightly enriched LREEs [$(La/Yb)_N$ = 5.23–13.1] with positive Eu anomalies (Eu/Eu* = 1.81–3.66), and strongly enriched LREEs [$(La/Yb)_N$ = 20.8–66.5] with negative Eu anomalies (Eu/Eu* = 0.58–0.63) (Fig. 6k). Multi-element patterns exhibit positive K and Sr, and negative Nb, P, and Ti anomalies (Fig. 6l).

Mid–Jurassic granitoids (~170 Ma). Porphyritic granitoids have SiO_2 values from 64.1 to 70.6 wt%, total alkalis from 8.31 to 9.47 wt%, and Al_2O_3 from 14.7 to 16.6 wt%. They show moderate TiO_2 (0.30–0.82 wt%), MgO (0.45–1.15 wt%), FeO^T (1.72–3.92 wt%), and Mg# (31.8–38.5). These granitoids are primarily quartz monzonite (Fig. 5a), fall into the shoshonitic series (Fig. 5b), and are of magnesian type (Fig. 5c), with weakly peraluminous characteristics (ASI = 1.01–1.06) (Fig. 5d). REE patterns show LREE enrichment [$(La/Yb)_N$ = 17.7–20.6] and negative Eu anomalies (Eu/Eu* = 0.49–0.60) (Fig. 6m). Multi-element patterns display negative anomalies in Nb, P, and Ti, with notable enrichment in Rb, K, and Pb (Fig. 6n).

4.4. *Mineral chemistry*

Seven representative samples from each group were selected for the EPMA analysis. Mineral formula recalculations were carried out using the MATLAB®-based MinPlot program (Walters, 2022). Representative mineral compositions and their structural formulas are presented in Supplementary Table S6. Detailed descriptions of feldspar, biotite, and amphibole chemistry are provided in Supplementary Document S1.

4.4.1. *Estimation of crystallization conditions*

Mafic hydrous minerals, such as amphibole and biotite, are essential constituents of many granitoid rocks. Their concurrent analysis can effectively constrain magma crystallization conditions (Czamanske and Wones, 1973). Biotite composition is particularly useful for estimating crystallization temperature (Henry et al., 2005) and depth (Uchida et al., 2007), while amphibole compositions also provide important constraints on granitic magma crystallization pressure–temperature conditions (Schmidt, 1992; Ridolfi et al., 2010). Numerous geothermobarometers have been developed, each requiring specific sample parameters for accurate estimation. In this study, representative samples with a wide range of mineral compositions were selected to estimate crystallization conditions. Some biotite and amphibole geothermobarometers were applied (Supplementary Document S1). Since some samples are amphibole-free, we primarily used biotite geothermobarometers to constrain pressure–temperature conditions; amphibole geothermobarometers were applied only for amphibole-bearing samples to validate the conditions determined from biotite (Table 3).

5. Tectonomagmatic evolution of the Ereendavaa Block in the Mongolian Collage context

5.1. *Timing of magmatism*

We report 271 concordant zircon dates from 16 granitoids, spanning from 160 to 1346 Ma. These ages, identified as magmatic based on CL zoning and high Th/U ratios (>0.1), show seven distinct magmatic episodes: Tonian (~880 Ma), late Ediacaran (~540 Ma), early Ordovician (~470 Ma), early Silurian (~440 Ma), late Triassic (~220 Ma), early Jurassic (~190 Ma), and middle Jurassic (~170 Ma). Zircon overgrowths from the ~880 Ma and ~540 Ma granitoids yield $^{206}Pb/^{238}U$ ages of 444 Ma and 451 Ma, respectively, which likely represent the timing of metamorphism during the Ordovician–Silurian. This metamorphism may have been triggered by magmatic events that occurred between 470 and 440 Ma (Fig. 4e–f). Minor age peaks at ~1.3 Ga, ~1.0 Ga, and ~300 Ma were also identified (Fig. 8). The inherited zircon ages at ~1.3 Ga and ~1.0 Ga are consistent with an igneous origin and closely correspond to the detrital zircon age spectra reported by Miao et al. (2020), which range from ~0.97 to ~1.42 Ga. Granitic intrusions dated to ~880 Ma reveal a previously undocumented Tonian magmatic episode within the EDB.

In addition to the newly identified Tonian magmatism, the EDB records a protracted magmatic history reflecting episodic crustal activity from the Neoproterozoic to the Mesozoic, which is well supported by this study and previous investigations (Supplementary Table S2). Ediacaran–early Cambrian magmatism is marked by ~540 Ma felsic intrusions, consistent with associated mafic to intermediate complexes emplaced between 557 and 518 Ma (Orolmaa et al., 2015) and a granite dated at 534 ± 7 Ma (Zhu et al., 2023a). Early Ordovician granitoids (~470 Ma) and coeval rhyolites (461–450 Ma) indicate regionally extensive igneous activity during this period (Narantsetseg et al., 2019; Miao et al., 2020). Early Silurian magmatism is constrained by ~440 Ma granitoids, corroborating prior geochronological data (Orolmaa et al., 2015; Miao et al., 2016). Inherited zircon ages around 300 Ma reflect late Carboniferous to early Permian magmatism, which is in agreement with zircon ages from metamorphic rocks (296–271 Ma; Daoudene et al., 2013; Miao et al., 2017). Late Triassic (~226–207 Ma) and Jurassic (~192–171 Ma) granitoids document continued Mesozoic magmatism, consistent with earlier reports of high-K calc-alkaline and mylonitic granitoids in the region (Tomurtogoo et al., 2005; Orolmaa et al., 2015; Miao et al., 2016).

5.2. *Characteristics of magmatism*

The major and trace element compositions of the studied granitoids vary significantly despite similar crystallization ages and mineral assemblages (Figs. 5, 6). As REEs remain immobile during low-grade alteration (McLennan, 1989; Bau, 1991), they are reliable for source

Table 3
Representative geothermobarometer calculations of the studied samples. Equations used for temperature–pressure calculations from: (1) Henry et al. (2005); (2) Li and Zhang (2022); (3) Otten (1984); (4) Blundy and Holland (1990); (5) Uchida et al. (2007); (6) Li and Zhang, (2022); (7) Schmidt (1992); (8) Mutch et al. (2016).

Representative sample	Temperature (°C)						Pressure (kbar)					
	Biotite			Amphibole			Biotite			Amphibole		
	max	min	Mean	max	min	Mean	max	min	Mean	max	min	Mean
Tonian granitoid	627	608	619$^{(1)}$				3.73	2.38	2.98$^{(5)}$			
(Sample 1001)	880	806	**853$^{(2)}$**				10.77	7.26	**8.53$^{(6)}$**			
Ediacaran granitoid	642	608	623$^{(1)}$	682	654	668$^{(3)}$	1.63	1.38	1.49$^{(5)}$	7.32	6.29	6.76$^{(7)}$
(Sample 1704D)	842	808	**825$^{(2)}$**	811	787	798$^{(4)}$	3.42	3.10	**3.22$^{(6)}$**	5.91	4.95	5.38$^{(8)}$
Ordovician granitoid (Sample 1205A)	592*	571*	630$^{(1)}$	689	653	676$^{(3)}$	2.43	1.97	2.19$^{(5)}$	7.28	7.00	7.10$^{(7)}$
	759	746	**753$^{(2)}$**	780	758	767$^{(4)}$	4.71	3.90	**4.20$^{(6)}$**	5.86	5.59	5.69$^{(8)}$
Silurian granitoid	698*	662*	676$^{(1)}$				3.39	3.17	3.28$^{(5)}$			
(Sample 1205B)	771	755	**762$^{(2)}$**				7.23	5.44	**6.38$^{(6)}$**			
Triassic granitoid	707	674	694$^{(1)}$	733	714	725$^{(3)}$	1.82	1.56	**1.68$^{(5)}$**	3.46	3.35	3.41$^{(7)}$
(Sample 1205B)	796	789	**791$^{(2)}$**	738	711	723$^{(4)}$	6.09	4.39	5.07$^{(6)}$	2.79	2.72	2.75$^{(8)}$
Early Jurassic granitoid (Sample 1201B)	695	675	682$^{(1)}$				2.20	1.80	2.00$^{(5)}$			
	803	795	**799$^{(2)}$**				6.86	5.43	**6.25$^{(6)}$**			
Mid–Jurassic granitoid (Sample 1403A)	707	692	701$^{(1)}$				1.40	1.31	1.37$^{(5)}$			
	801	796	**799$^{(2)}$**				3.72	3.35	**3.55$^{(6)}$**			

Equations used for temperature and pressure calculations:
(1) $T(°C) = [(\ln Ti + 2.3594 + 1.7283 \times (X_{Mg})^3)/(4.6482 \times 10^{-9})]^{0.333}$.
(2) Machine Learning Thermobarometry (https://lixiaoyan.shinyapps.io/Biotite_thermobarometer/).
(3) $T(°C) = 1204 \times (Ti/23O) + 545$.
(4) $T(°K) = (0.677 \times P(Kbar) - 48.98 + Y)/(-0.0429 — 0.008314 \times \ln X_{ab})$.
(5) $P(kbar) = 3.03 \times Al^T - 6.53$.
(6) Machine Learning Thermobarometry (https://lixiaoyan.shinyapps.io/Biotite_thermobarometer/).
(7) $P(kbar) = -3.01 + 4.76 \times Al^T$.
(8) $P(kbar) = 0.5 + 0.331 \times Al^T + 0.995 \times (Al^T)^2$.
* Out of calibration range or specified condition.

interpretation. Tonian (~880 Ma), Ediacaran (~540 Ma), Silurian (~440 Ma), and early Jurassic (~190 Ma) granitoids display two distinct REE patterns (Fig. 6). To constrain source characteristics, we selected unfractionated or weakly fractionated samples, which better preserve primary signatures (Whalen et al., 1987; Wu et al., 2017). Tonian granitoids (~880 Ma) and sample 1704D from the Ediacaran granitoids (~540 Ma) are predominantly unfractionated (Fig. 9a). In contrast, most Silurian (~440 Ma) granitoids are fractionated, except for samples 1205B and 1602 (Fig. 9b). Among the early Jurassic (~190 Ma) granitoids, sample 1105 is notably fractionated, whereas others are not. Following the criteria of Wu et al. (2017), only unfractionated or weakly fractionated samples are used to infer magma sources.

5.2.1. *Tonian magmatism (~880 Ma)*

Petrogenetic implications

The Tonian leucogranitoids (~880 Ma) are largely unfractionated and display two distinct REE patterns (Fig. 6a). Negative Eu and Ba anomalies likely reflect K-feldspar fractionation, while Nb–Ti–P troughs suggest the involvement of Ti-bearing phases and apatite (Fig. 6a–b). These peraluminous granitoids (ASI = 1.05–1.26), with enriched LREEs [$(La/Yb)_N$ = 7.69–22.9], contain primary biotite (Fig. 7c) and exhibit emplacement conditions of ~ 8.5 kbar and 853 °C, consistent with mid-crustal crystallization (~28 km depth). Eu anomalies vary, from strongly negative (Eu/Eu* = 0.21 in 1101B) to slightly positive (up to 1.70), likely due to feldspar accumulation or crustal contamination. Their calc-alkaline to high-K affinity and enrichment in Rb, K, and Pb suggest partial melting of aluminum-rich crust in a continental setting.

Magma source and tectonic setting

The geochemical features of the Tonian granitoids suggest derivation through (1) partial melting of aluminum-rich (meta-)sedimentary rocks, such as metapelites and metagraywackes (Patiño Douce, 1999; Eyal et al., 2004; Healy et al., 2004), or (2) partial melting of (meta-)igneous rocks like tonalite or granodiorite at pressures >8 kbar, involving residual restitic phases (Patiño Douce, 1999). The abundance of inherited zircons and scarcity of mafic minerals support a dominant sedimentary source. Source identification using the Al–Fe–Mg–Ti–Ca system (Fig. 9c) points to a pelitic origin for high-REE granitoids (e.g., 1101B) and a greywacke source for low-REE samples (e.g., 1001). Comparable ~880 Ma I-type granitoids in the Manzhouli area (NE China) are interpreted as products of deep-seated basaltic underplating (Gou et al., 2013), contrasting with the mid-crustal S-type granitoids in this study. A similar two-source model is observed in ~15 Ma I- and S-type granitoids formed under extension from both lower crustal igneous and mid-crustal sedimentary sources (Lamont et al., 2023). Regional rifting during the early Neoproterozoic has also been proposed for the Ereendavaa Block (Miao et al., 2020). Although the granitoids plot in both arc-related (VAG) and *syn*-collisional (*syn*-COLG) fields (Fig. 9e–f), these distributions likely reflect inherited source characteristics rather than active subduction (Pearce et al., 1984). Integrated evidence suggests that the Tonian granitoids (~880 Ma) were likely derived as S-type magmas from (meta-)sedimentary crust in an extensional setting.

5.2.2. *Late Ediacaran magmatism (~540 Ma)*

Petrogenetic implications

Sample 1704D, with a hornblende-bearing assemblage, likely represents an unfractionated granodiorite (Fig. 9a). The associated hornblende-absent granites display features of fractional crystallization, including negative Eu anomalies and low Ti and P (Fig. 6c–d), consistent with the removal of apatite, amphibole, and feldspar. Amphibole in 1704D is pargasite (Fig. 7g), indicating equilibrium with calc-alkaline melts (Ridolfi and Renzulli, 2012; Pál-Molnár et al., 2015), and biotite chemistry reflects a similar calc-alkaline signature (Fig. 7d–e), consistent with the whole-rock composition (Fig. 5b).

Magma source and tectonic setting

Calc-alkaline metaluminous granites may form via fractional crystallization of mantle-derived basalt, magma mixing, or partial melting of juvenile mafic crust (Chappell and White, 2001; Kemp et al., 2007; Clemens et al., 2011; Moyen et al., 2017). However, the absence of mafic enclaves (Chappell, 1996) and the lack of a strong Eu anomaly in sample 1704D argue against magma mixing or a mantle-derived basaltic source. Instead, its unfractionated nature supports an origin by the partial melting of juvenile mafic crust. This interpretation is supported by experimental melts of mafic to ultramafic rocks (Fig. 9d), hornblende-rich mineralogy indicating water-rich conditions (Sisson et al., 1996),

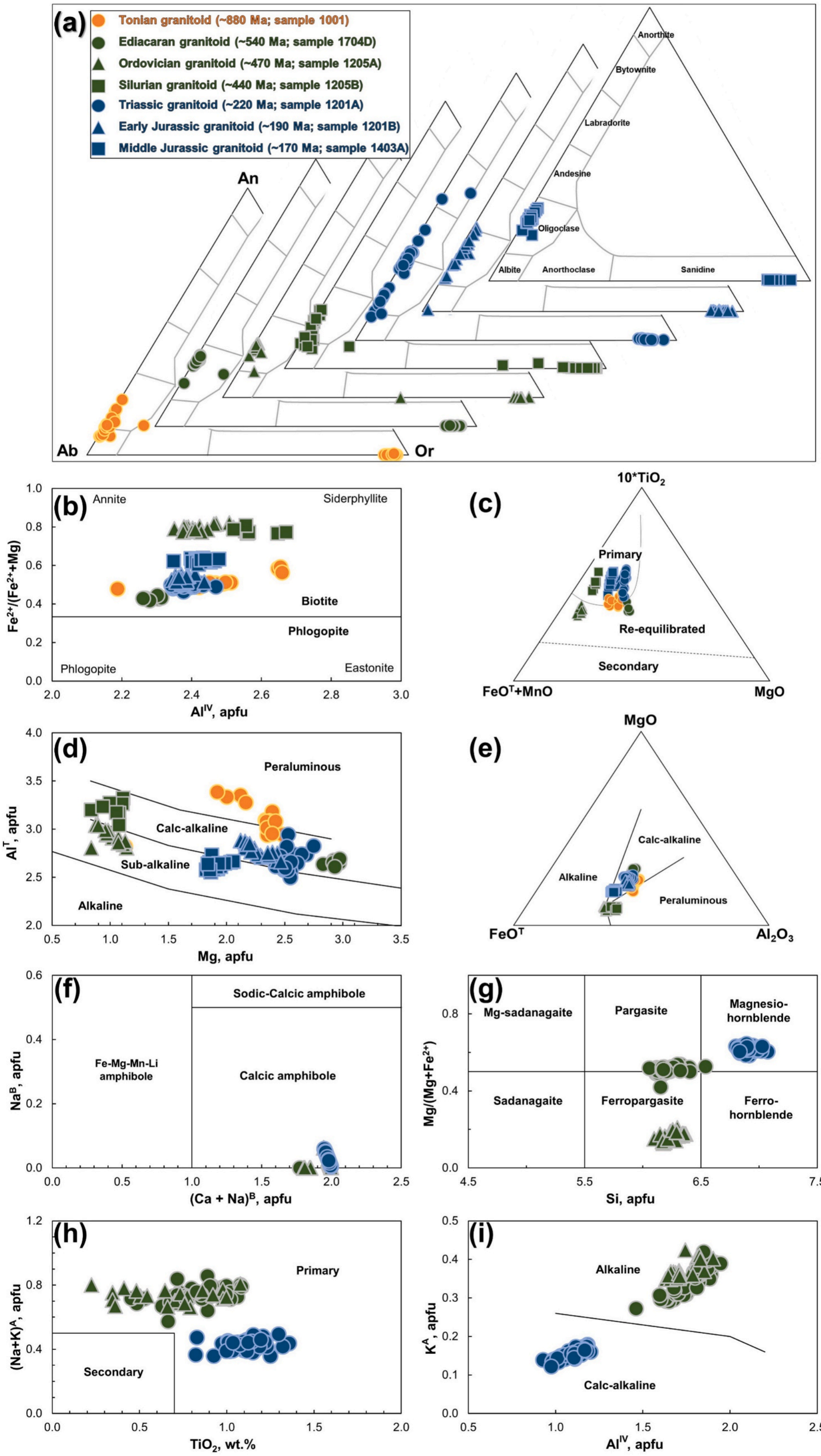

(caption on next page)

Fig. 7. (a) An–Ab–Or ternary cation diagram for feldspars (after Deer et al., 1992). Abbreviations: Ab-albite, An-anorthite, Or-orthoclase. (b) Al^{IV} versus $Fe^{+2}/(Fe^{2+}+Mg)$ plot for biotite (after Deer et al., 1992). (c) (10xTiO_2) – (FeO^T + MnO) – MgO ternary diagram for primary and secondary biotite (after Nachit et al., 2005). (d) Al^T versus Mg plot for biotite (after Nachit et al., 1985). (e) MgO–FeO–Al_2O_3 ternary diagram for source classification of biotite (after Abdel-rahman, 1994). (f) Na^B versus $(Ca + Na)^B$ plot for amphibole (after Leake et al., 1997). (g) $Mg/(Mg + Fe^{2+})$ versus Si classification diagram for calcic amphiboles (after Leake et al., 1997). (h) $(Na + K)^A$ versus TiO_2 classification diagram for primary and secondary amphibole (after Molina et al., 2009). (i) K^A versus Al^{IV} discrimination diagram for source of amphibole (after Ridolfi and Renzulli, 2012).

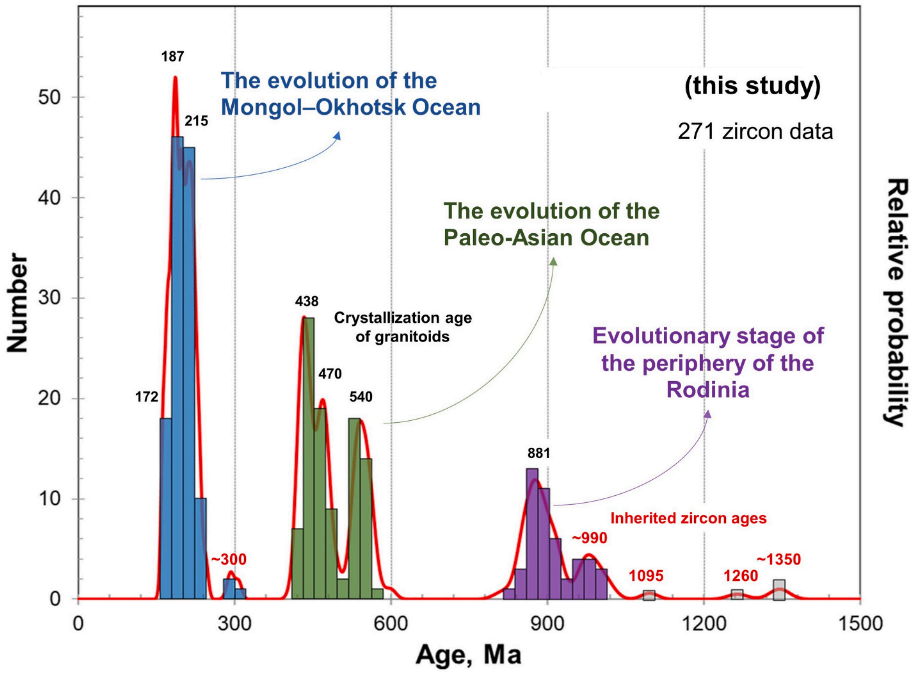

Fig. 8. Histogram and relative probability plot of zircon U–Pb ages from the dated samples in this study. Age data are provided in Supplementary Table S4.

and arc-type signatures in discrimination diagrams (Fig. 9e–f). Therefore, we propose that the Ediacaran granitoids (~540 Ma) formed through partial melting of juvenile mafic crust that had been metasomatized by slab-derived fluids in a subduction-related arc setting, rather than being directly derived from slab melts.

5.2.3. *Early Ordovician magmatism (~470 Ma)*

Petrogenetic implications

The ~470 Ma granitoids exhibit high-K calc-alkaline, magnesian, and peraluminous signatures. Their high silica content (72–82 wt%) and negative Eu anomalies suggest significant fractional crystallization. Mineralogical evidence from sample 1205A supports this interpretation, as it contains abundant hydrous mafic minerals. Amphiboles are classified as ferropargasite (Fig. 7g), a composition typical of alkaline magmatic systems (Fig. 7i; Pál-Molnár et al., 2015; Ridolfi and Renzulli, 2012), while associated biotites show a slightly alkaline trend (Fig. 7d–e), indicating a possible alkaline component in the source.

Magma source and tectonic setting

The elevated Mg, Ni, and Cr contents, along with experimental data (Fig. 9d), suggest that the Ordovician granitoids may have formed via partial melting of mafic to ultramafic sources. Their crust-like REE patterns, negative Eu anomalies, LILE enrichment, and HFSE depletion imply significant crustal input. While arc-related rhyolites (~460 Ma) are reported from the southern EDB (Narantsetseg et al., 2019), the granitoids in Bayanmod, Airgin-Enger, and Ereet-Uul likely reflect magmatism in an extensional regime within the central part of the EDB, possibly linked to early-stage continental rifting (Luo et al., 2018). A similar tectonic shift—from arc (~485 Ma) to extensional (~466 Ma) settings—has been documented in the neighboring Erguna Block and attributed to slab rollback (Nicolosi et al., 2006; Zhou et al., 2015; Gou et al., 2019). This interpretation is further supported by LP metamorphism at 477 ± 15 Ma (Sergelen, 2018), typical of back-arc basins (Thompson et al., 2001). Collectively, these observations support a back-arc extensional setting for the Ordovician granitoids in the EDB.

5.2.4. *Early Silurian magmatism (~440 Ma)*

Petrogenetic implication

The Silurian granitoids exhibit geochemical features suggestive of advanced fractional crystallization (Fig. 9a), though samples 1205B and 1602 may reflect less evolved sources (Fig. 9b). Their high SiO_2 and Al_2O_3, low MgO and Ni, and LILE enrichment with HFSE depletion suggest derivation from evolved felsic crust. Variations in Eu anomalies—weak in 1205B, stronger in 1602—likely reflect differential plagioclase fractionation. The mineralogical features of sample 1205B, including the presence of primary biotite (Fig. 7b–c), are in agreement with whole-rock chemistry and may point to an S-type affinity. Biotite compositions reflect a calc-alkaline, peraluminous nature (Fig. 7d–e), and geothermometry yields ~762 °C, consistent with low-temperature crystallization of S-type granites (White and Chappell, 1988; Sylvester, 1998). Overall, these features imply derivation from continental crust-like sources (Taylor and McLennan, 1985).

Magma source and tectonic setting

Experimental constraints suggest a pelitic source for sample 1205B and greywacke for 1602 (Fig. 9c). Despite ambiguous positioning in tectonic discrimination diagrams (Fig. 9e–f), likely due to source-inherited geochemical imprints (Pearce et al., 1984), the granitoids exhibit features consistent with S-type granites, which can form in various tectonic settings—arc, collisional, back-arc, or post-collisional (Sylvester, 1998; Barbarin, 1999; Collins and Richards, 2008; Jiang et al., 2011). Regional evidence points to subduction-related activity during the Cambrian–Ordovician (e.g., Miao et al., 2017), with

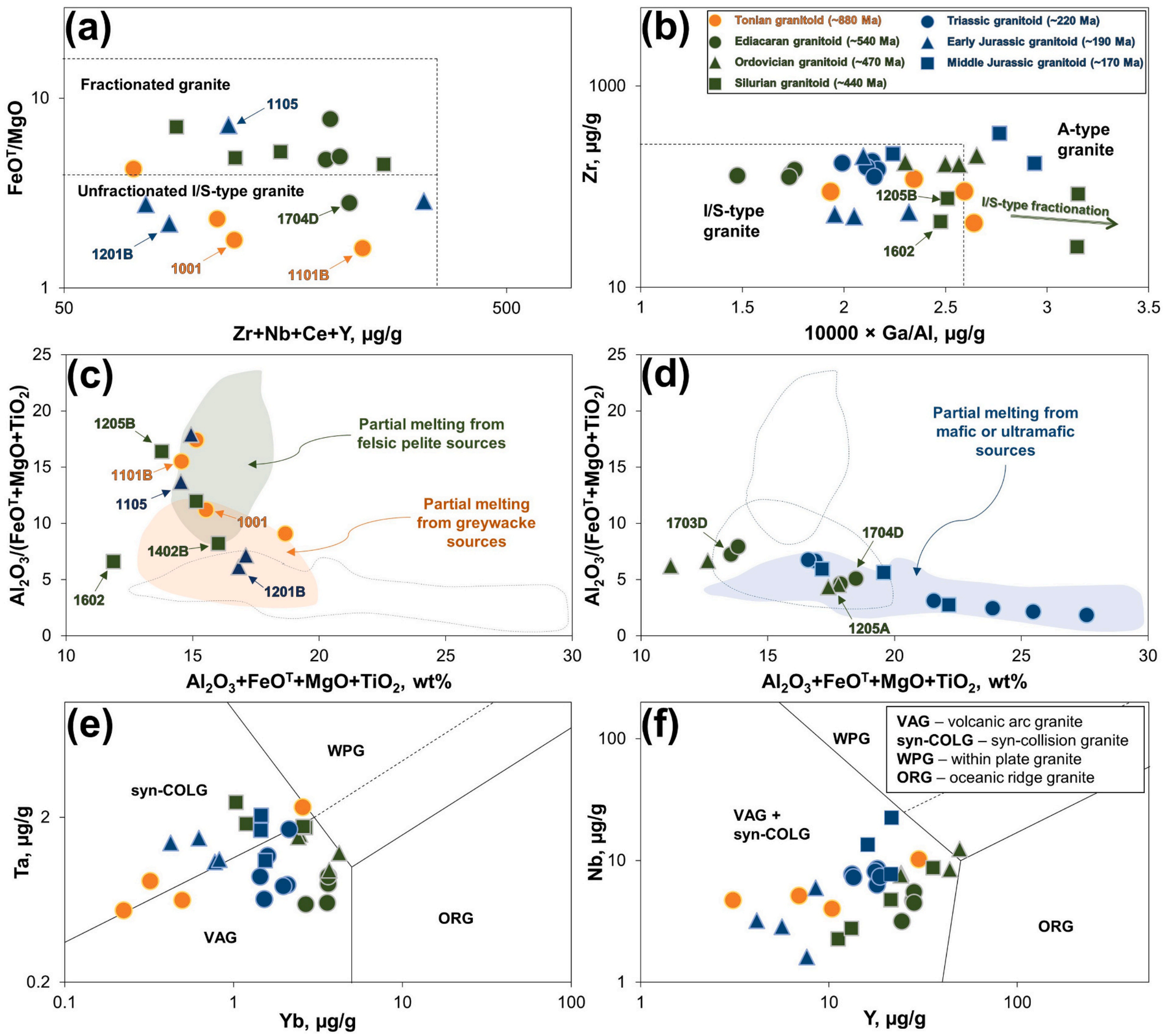

Fig. 9. (a) FeO^T/MgO versus Zr + Nb + Ce + Y plots for fractionated and unfractionated granites (after Whalen et al., 1987); (b) Zr versus 10000 x Ga/Al diagram for fractionated granites (after Wu et al., 2017); (c–d) Al-Fe-Mg-Ti-Ca diagram for a source of granitic melt (after Patiño Douce, 1999); (e) Ta versus Yb discrimination diagram for the tectonic setting of granite (after Pearce et al., 1984); (f) Nb versus Y discrimination diagram for granite (after Pearce et al., 1984).

continued PAO evolution into the early Silurian (e.g., Feng et al., 2018; Narantsetseg et al., 2019). We interpret the ~440 Ma granitoids as products of crustal melting under extensional back-arc conditions, potentially linked to slab rollback and lithospheric thinning. This process may have also driven the contemporaneous emplacement of ~440 Ma A-type, within-plate, fluorite-rich alkali granite (author's unpublished data). The presence of Fe-rich biotite (Fig. 7b) supports low-pressure crystallization in such extensional settings, possibly facilitated by rapid magma ascent and enhanced Fe incorporation into biotite.

5.2.5. Late Triassic magmatism (~220 Ma)

Petrogenetic implication

The Triassic granitoids (~220 Ma) are characterized by biotite–hornblende assemblages, with MMEs and accessory phases like titanite, allanite, and magmatic epidote (Fig. 3m, o), suggesting an I-type affinity (Petrik et al., 1994; Chappell and White, 2001). They range from diorite to granite, with metaluminous to weakly peraluminous, high-K calc-alkaline, and magnesian compositions (Fig. 5a–d). Primary biotite (Fig. 7c) and calcic amphibole (Fig. 7h, 7d–e, 7i), mainly magnesio-hornblende (Ridolfi and Renzulli, 2012; Pál-Molnár et al., 2015), support a calc-alkaline lineage. Moderate Eu anomalies (Eu/Eu* = 0.62–0.68) and low Ti and P (Fig. 6i–j) suggest fractional crystallization of apatite, amphibole, and feldspar, contributing to the evolution of hornblende-poor, weakly peraluminous I-type granites (Chappell et al., 2012).

Magma source and tectonic setting

The I-type signature of the Triassic granitoids (~220 Ma) suggests partial melting of (meta-)igneous mafic to ultramafic protoliths (Fig. 9d), with limited fractional crystallization. Their hydrous mineral assemblage—including hornblende, biotite, and magmatic epidote—indicates crystallization from water-rich magmas (Sisson et al., 1996). The presence of MMEs (Fig. 3m), more mafic than their host, reflects magma mixing via mafic injections into felsic magma chambers. Such mingling processes are typical in subduction-related arcs (Chappell, 1996; Suzaño et al., 2017), consistent with tectonic discrimination diagrams (Fig. 9e–f; Pearce et al., 1984). We interpret these granitoids as products of I-type magmatism from a hybrid source involving mantle-derived mafic magma and slab-derived components, emplaced in an arc-related setting.

5.2.6. Early Jurassic magmatism (~190 Ma)

Petrogenetic implication

The Early Jurassic granitoids (~190 Ma) can be classified into two groups: one (e.g., sample 1105) with high REE content and pronounced negative Eu anomalies (La/Yb_N = 20.8–66.5; Eu/Eu* = 0.58–0.63), and another (e.g., sample 1201B) with lower REE concentrations and positive Eu anomalies (La/Yb_N = 5.23–13.1; Eu/Eu* = 1.81–3.66), likely reflecting plagioclase removal and accumulation. The presence of muscovite and metasedimentary xenoliths (Fig. 3f), along with a biotite crystallization temperature of ~799 °C, supports an S-type affinity (White and Chappell, 1988; Sylvester, 1998).

Magma source and tectonic setting

These granitoids are best classified as S-type granites, likely derived from (meta-)sedimentary sources. High-REE samples suggest pelitic origins, while low-REE types point to greywacke (Fig. 9c). Shared features—enriched LREEs, flat HREEs, LILE enrichment, and HFSE depletion—indicate a continental crustal source (Taylor and McLennan, 1985). These geochemical traits and their positions on tectonic discrimination plots (Fig. 9e–f) suggest formation in a collisional tectonic setting.

5.2.7. Middle Jurassic magmatism (~170 Ma)

Petrogenetic implication, magma source, and tectonic setting

The ~170 Ma granitoids, characterized as quartz monzonite with shoshonitic, magnesian, and slightly peraluminous compositions (Fig. 5a–d), lack peraluminous minerals such as cordierite, garnet, and muscovite (Fig. 3u), which may suggest a non-sedimentary origin. Their geochemical signatures, including enrichment in LILEs and depletion in HFSEs, indicate a derivation from a crustal protolith. In contrast to melts derived from pelitic and greywacke sources, their compositions align with those produced from mafic or ultramafic sources (Fig. 9d). Discrimination plots do not clearly define a specific tectonic setting for these granitoids, as they plot within both volcanic arc and *syn*-collisional fields (Fig. 9e–f). However, post-collisional granites can also display arc-like trace element signatures due to the influence of subduction-related materials from previous tectonic events (e.g., Ganbat et al., 2021). The timing of ~170 Ma has been associated with the closure of the Mongol-Okhotsk Ocean (Tomurtogoo et al., 2005). Therefore, we propose that these granitoids may be derived from crustal igneous rocks, likely in a post-collisional setting.

6. Geological history of the wandering Mongolian Collage

6.1. Basement of the Mongolian Collage

The oldest crustal remnants in the Mongolian Collage occur in the Gargan, Tarvagatai, Zavkhan, Baydrag, and Ereendavaa-Erguna Blocks, where Neoarchean to Paleoproterozoic basement rocks (2.70–1.97 Ga) have been documented (Fig. 1b; Khain et al., 2002; Kozakov et al., 2007; Demoux et al., 2009a, 2009b; Kröner et al., 2010; Kozakov et al., 2011; Kuzmichev and Larionov, 2013; Kröner et al., 2015; Bold et al., 2016a; Buriánek et al., 2017; Bold et al., 2019; Kovach et al., 2019; Miao et al., 2020; Skuzovatov, 2021; Feng et al., 2022). In contrast, the Tsagaan Uul and Khutag Uul Blocks consist of Tonian granitic gneisses (~0.95–0.92 Ga; Fig. 1b) and lack older zircon signatures (Yarmolyuk et al., 2005; Wang et al. (2001), suggesting a distinct crustal evolution. A prominent inherited and detrital zircon population centered at ~1.85 Ga is widespread across multiple Blocks (Fig. 10a), including Baydrag (Demoux et al., 2009a), Tarvagatay (Kröner et al., 2015), Erguna (Feng et al., 2022), Zavkhan, Gargan, and Ereendavaa (Kovach et al., 2019; Bold et al., 2019; Miao et al., 2020). This age is broadly interpreted as reflecting HT metamorphism and magmatism linked to the assembly of the Columbia supercontinent (Zhao et al., 2004). Comparable ~1.85 Ga events are reported in the South Siberian post-collisional belt (e.g., Donskaya and Gladkochub, 2021), Angara belt (Priyatkina et al., 2018), North Tarim (Xu et al., 2013), and the Trans-North China Orogen (Lu et al., 2008), where it marks the amalgamation of the craton's Eastern and Western Blocks. In Siberia and Tarim, the same age is regarded as indicative of a major collisional event (e.g., Donskaya et al., 2014; Gladkochub et al., 2019; Wang et al., 2020), which may suggest the Mongolian Collage may have shared in this Paleoproterozoic tectonothermal history.

In addition, this study identifies a population of inherited zircons dated at ~1.3 Ga (Fig. 8), consistent with detrital zircon records from the Mongolian Collage (Zhou et al., 2018; Collett et al., 2024). Older ~1.6 Ga orthogneiss has been reported south of the Baydrag Block, beneath the Alag Khadny Unit in the Lake Zone (Skuzovatov, 2021), suggesting that these events represent a distinct tectonothermal history from those associated with the breakup of the Columbia supercontinent (~1.3 Ga; Zhao et al., 2011). The ~1.3 Ga age is widely interpreted as reflecting mantle plume activity and continental rifting, as evidenced by the emplacement of mafic dykes in southern Siberia (Donskaya et al., 2018) and the anorogenic granitoids in the Yenisey Ridge (Popov et al., 2010; Likhanov et al., 2012). In contrast, this age signal is largely absent in northern Tarim (Xu et al., 2013; Zhu et al., 2021), suggesting that the region may have rifted away from Siberia prior to this magmatic event (Wang et al., 2020). The persistence of inherited and detrital ~1.3 Ga zircons in the MCMs thus supports a prolonged tectonic connection to southern or western Siberia (Collett et al., 2024; Soejono et al., 2025), rather than to northern Tarim.

6.2. Evolutionary stage of the periphery of the Rodinia supercontinent and breakup

The ~1.0 Ga zircon-forming event identified in this study (Fig. 8) is generally interpreted as reflecting the assembly of the Rodinia supercontinent (Hoffman, 1991; Li et al., 2008). Both Siberian and Tarim cratons are reconstructed along Rodinia's periphery (Li et al., 2008; Pisarevsky et al., 2008; Kheraskova et al., 2010; Levashova et al., 2011; Cawood et al., 2016; Merdith et al., 2017). Magmatic and metamorphic events at ~1 Ga are extensively documented across the MCMs (Fig. 10a; Demoux et al., 2009b; Bold et al., 2019; Liu et al., 2020; Kovach et al., 2021; Feng et al., 2022), including Lake Zone (Fig. 10a; Badarch et al., 2002; Khain et al., 2002; Kröner et al., 2010; Kuzmichev and Larionov, 2013; Buriánek et al., 2017; Skuzovatov, 2021). The Khutag Uul and Tsagaan Uul Blocks in southern Mongolia (Fig. 10a; Wang et al., 2001; Yarmolyuk et al., 2005) may have coevolved with or remained distinct from the Mongolian Collage since ~1 Ga, although their tectonic affiliation remains unclear. In western Siberia, the Yenisei Ridge hosts adakite-like granitoids (~930–910 Ma; Likhanov et al., 2022), metabasites (~1183–1087 Ma; Likhanov et al., 2015), and granitic gneisses (~1100–950 Ma; Likhanov et al., 2014; Nozhkin et al., 2011). These findings suggest late Mesoproterozoic to early Neoproterozoic arc activity and a possible correlation between the Mongolian Collage and the western Siberian Craton.

The breakup of Rodinia and the geodynamic significance of its peripheral microcontinents remain topics of ongoing debate (e.g., Kuzmichev et al., 2001; Gladkochub et al., 2010; Levashova et al., 2010; Glorie et al., 2014). In this study, the ~880 Ma S-type granitoids of the EDB are interpreted as products of extensional or rift-related magmatism, coeval with the emergence of And- and Sil-bearing pelitic gneisses (Sergelen, 2018). Widespread HT/LP metamorphism and magmatism during ~880–860 Ma in the Baydrag (Štípská et al., 2023; Collett et al., 2024), Zavkhan (Kozakov et al., 2012, 2014, 2017), and Gargan Blocks (Bold et al., 2019) (Fig. 10a). In western Siberia, Yenisey Ridge records ~880–857 Ma S-type granitoids and related contact metamorphism (e.g., Vernikovskaya et al., 2002; Vernikovsky et al., 2007; Likhanov et al., 2014; Nozhkin et al., 2015, 2023), as well as LP metamorphism (Likhanov, 2022). HT/LP metamorphism is typically linked to crustal thinning in continental rift or back-arc settings (e.g., Thompson et al., 2001). These magmatic and metamorphic activities during ~880–860 Ma may be the record a regional extensional regime associated with early lithospheric thinning along the periphery of Rodinia, with temporal and geodynamic parallels indicating a tectonic linkage between the Mongolian Collage and western Siberia (Fig. 11a). In addition, the

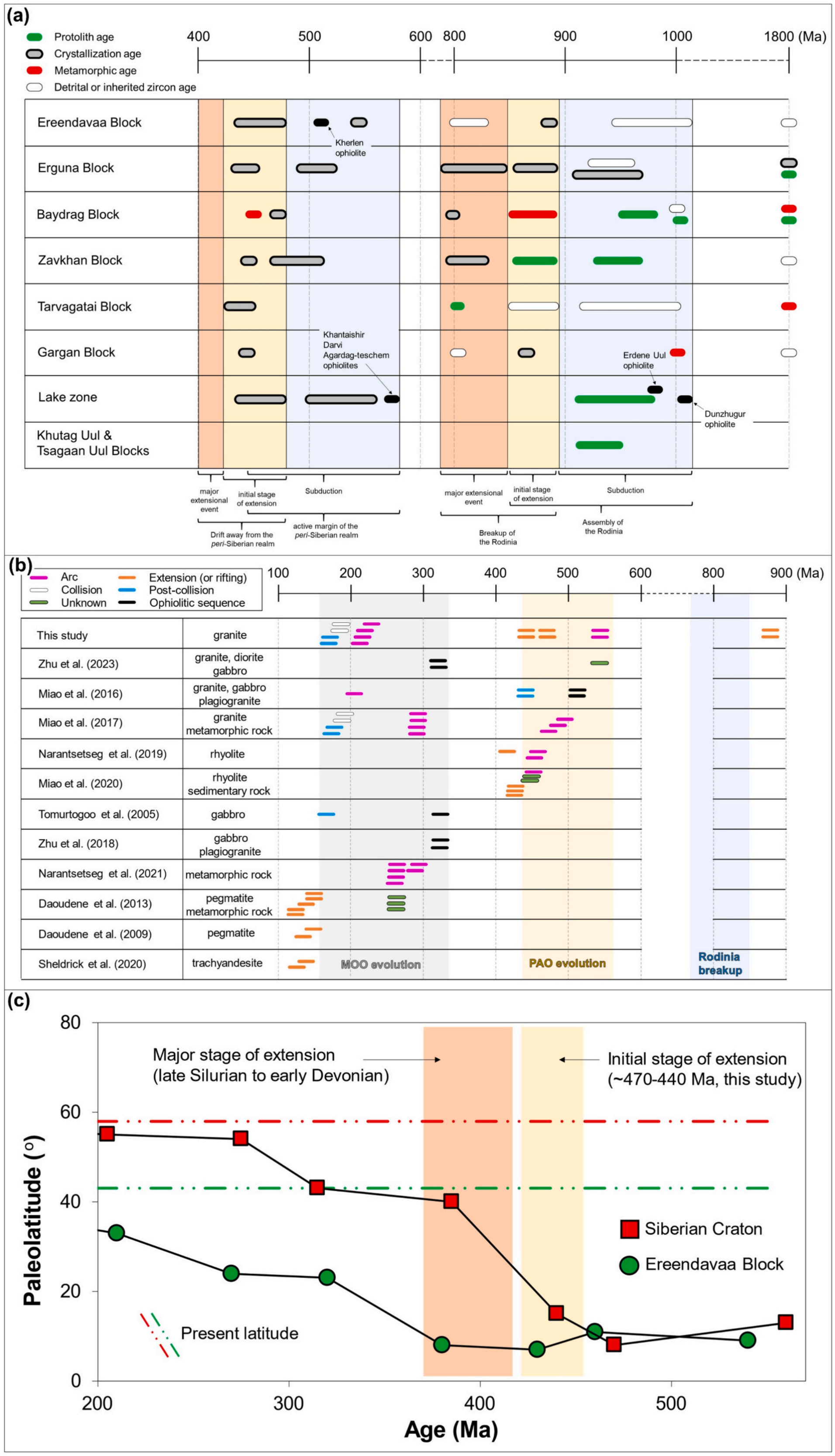

Fig. 10. (a) Compilation of zircon radiometric ages documented from microcontinents in Mongolia (data sources listed in Supplementary Table S1). (b) Summary of published radiometric ages from the Ereendavaa Block. The dataset is compiled in Supplementary Table S2 and includes sources from 2) Orolmaa et al. (2015); 3) Zhu et al. (2023a); 4) Miao et al. (2016); 5) Miao et al. (2017); 6) Narantsetseg et al. (2019); 7) Miao et al. (2020); 8) Tomurtogoo et al. (2005); 9) Zhu et al. (2018); 10) Narantsetseg et al. (2021); 11) Daoudene et al. (2013); 12) Daoudene et al. (2009); and 13) Sheldrick et al. (2020). (c) Paleozoic to Mesozoic paleolatitudinal positions of the Ereendavaa Block and Siberian Craton (Bretshtein and Klimova, 2007; Liu et al., 2021; Zhu et al., 2024).

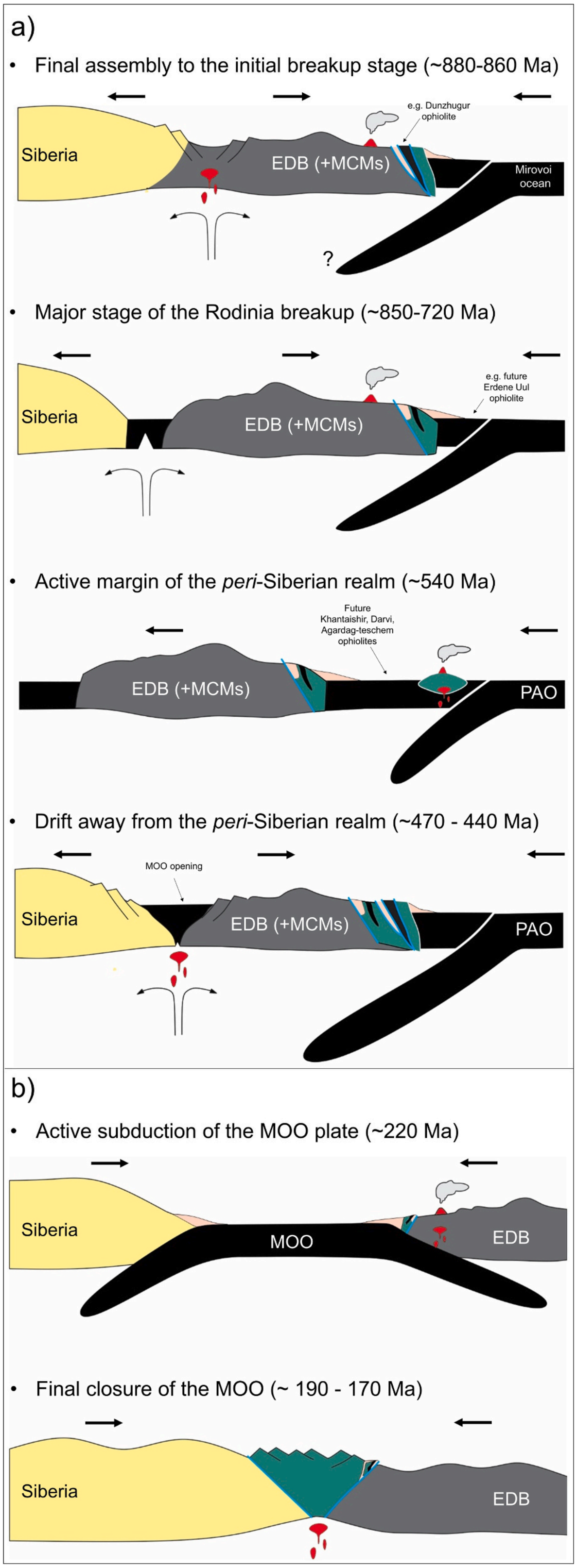

Fig. 11. Simplified tectonic model of the Ereendavaa Block showing: (a) evolution from ~880 to ~440 Ma with other Mongolian Collage microcontinents, and (b) independent evolution from ~220 to 170 Ma, playing a key role in the closure of the Mongol–Okhotsk Ocean. Modified from Cocks and Torsvik, (2007), Bold et al. (2016a, 2019), Miao et al. (2016, 2017), Safonova et al. (2017), Narantsetseg et al. (2019), Štípská et al. (2023), Soejono et al. (2023), and Zhu et al. (2023a).

late Tonian magmatic activities (~840–720 Ma) have been widely documented in both the Yenisei Ridge, western Siberia (e.g., Vernikovskaya et al., 2003, 2007; Likhanov and Reverdatto, 2015; Priyatkina et al., 2018) and the Mongolian Collage (e.g., Soejono et al., 2023 and references therein), and are attributed to a continental rifting event along Rodinia's passive margin (e.g., Levashova et al., 2010; Bold et al., 2016a; Soejono et al., 2023, 2025). This passive margin is believed to have been connected to the Rodinia breakup (e.g., Pisarevsky and Natapov, 2003; Ernst et al., 2008; Li et al., 2008), which ultimately led to the formation of the PAO (e.g., Cawood, 2005).

6.3. Development of the peri-Siberian continental arc system and subsequent rifting

After rifting from western Siberia (Fig. 11a), most MCMs underwent dextral translation along the Siberian margin and were subsequently re-accreted to its southern flank during the late Ediacaran to early Paleozoic (e.g., Soejono et al., 2025). Meanwhile, small-scale subduction systems progressively amalgamated individual Blocks through the late Neoproterozoic to the earliest Cambrian (e.g., Sukhbaatar et al., 2024), reflecting a complex, multi-phase tectonic assembly. This study documents ~540 Ma I-type magmatism (Fig. 10b) in an arc setting along the southern margin of the EDB (Fig. 1b), with granitic exposures closely associated with the late Cambrian (~500 Ma; Miao et al., 2016) Kherlen ophiolitic complex in the field. This area is classified as the Kherlen terrane (Badarch et al., 2002), initially developed as an intra-oceanic arc system during the Ediacaran–early Cambrian period (Narantsetseg et al., 2019). Therefore, ~540 Ma I-type magmatism may have played a significant role in the development of the late Neoproterozoic–early Cambrian intra-oceanic arc system (Narantsetseg et al., 2019). Similarly, the late Ediacaran (~570 Ma) ophiolitic and Cambrian–Ordovician magmatic arc complexes are widely distributed across the Mongolian Collage (Figs. 1b and 10a). The similar formation ages of the ophiolitic complexes suggest that the subduction of PAO plate(s) beneath most MCMs was likely initiated at ~570 Ma, contributing significantly to the development of the Cambrian–Ordovician Ikh Mongol arc system (Fig. 11a; Janoušek et al., 2018). These complexes are centered along the outer periphery of the Baydrag and Zavkhan Blocks in western Mongolia (Rudnev et al., 2009, 2012, 2013; Izokh et al., 2011; Yarmolyuk et al., 2011; Kovalenko et al., 2014; Buriánek et al., 2017; Janoušek et al., 2018; Buriánek et al., 2022; Sukhbaatar et al., 2022; Soejono et al., 2023). Furthermore, in the eastern continuation of the EDB in northeastern China and far-east Russia, Cambrian–Ordovician magmatic complexes are also widely distributed (e.g., Wu et al., 2011; Sorokin et al., 2017). The Ikh-Mongol arc system likely formed during large-scale subduction of the PAO beneath southern microcontinents and may have contributed to the accretion of Rodinia-derived Blocks to the southern margin of the Siberian Craton (e.g., Donskaya et al., 2000; Gladkochub et al., 2008; Li et al., 2023)

Our findings from the southern edge of the EDB, potentially linked to the Ikh Mongol Arc system, are not confined to the EDB but are extensively documented across other microcontinents in Mongolia and the eastern continuation of the EDB. This widespread magmatism suggests that these microcontinents may have undergone a similar tectono-magmatic evolution during the Cambrian–Ordovician period. It is plausible that the MCMs were either interconnected within a shared geodynamic environment following the breakup of Rodinia or developed independently but within a comparable tectonic regime. The pervasive magmatic activity along the outer periphery of the MCMs (including Ereendavaa-Erguna Block) further supports the presence of an active continental margin within the *peri*-Siberian realm during this time, likely linked to ongoing subduction and arc-related processes, within the broader context of the central-eastern CAOB.

In this study, we propose that the EDB experienced two stages of back-arc extensional magmatism during the Ordovician–Silurian period (Fig. 10b), triggered by the successive subductions of the PAO beneath the EDB. These back-arc magmatism may have occurred concurrently with the previously documented arc-related magmatic activity (Fig. 10b; e.g., Narantsetseg et al., 2019). Evidence of rifting and extension-related magmatism during the Ordovician–Silurian period is found in the Zavkhan (~442 Ma), Tarvagatai (~440 Ma), Gargan (~437 Ma), and Erguna (~440 Ma) Blocks (Fig. 10a; Kozakov et al., 2011; Bold et al., 2016a, 2019; Feng et al., 2018). Magmatism in the Baydrag Block occurred at ~470 Ma (Demoux et al., 2009a), followed by regional metamorphism at ~450 Ma (Kurimoto et al., 1998), while the Lake Zone also experienced ~470–440 Ma alkalic magmatism (Yarmolyuk et al., 2011 and references therein). An extensional regime developed in the Altai Wedge at ca. 435 Ma along the western margin of the Lake Zone, as indicated by metamorphic, magmatic, and structural evidence, and is interpreted to reflect slab rollback related to subduction of the PAO (e.g., Soejono et al., 2021). The widespread Ordovician–Silurian geochronological, magmatic, and metamorphic data (Fig. 10a) suggest a coherent pattern of back-arc extensional magmatism across the Mongolian Collage, offering strong support for paleogeographic models of the Mongolian Collage during this period (Domeier and Torsvik, 2014; Kilian et al., 2016). The interpretation is further corroborated by paleomagnetic constraints (Fig. 10c; Bretshtein and Klimova, 2007; Kravchinsky et al., 2010), paleontological correlations (Cocks and Torsvik, 2007), and sedimentary records (e.g., Miao et al., 2020), collectively reinforcing a tectonic model involving widespread back-arc extension along the southern margin of the Siberian realm during the Ordovician–Silurian. The extension-related evolution of the EDB during the Ordovician–Silurian (~470–440 Ma) bears a striking resemblance to the processes that initiated the breakup of Rodinia at ~880 Ma. The breakup of Rodinia occurred ~60 Ma before its main rifting episode (~825–750 Ma). Drawing on this comparison, we propose a similar tectono-magmatic model for the Ordovician–Silurian evolution of the EDB and other MCMs. This phase likely represents the early stages of continental extension, which led to the rifting of the Mongolian Collage from Siberia (Fig. 11a; e.g., Bold et al., 2019). The final stage of rifting may be associated with a large-scale extensional event during the late Silurian to early Devonian (e.g., Narantsetseg et al., 2019; Soejono et al., 2021; Zhu et al., 2024), a process that has also been linked to the opening of the Mongol-Okhotsk Ocean (e.g., Kurihara et al., 2009; Bussien et al., 2011; Zhu et al., 2024).

6.4. Evolution of the Mongol-Okhotsk Ocean

The MOO is widely proposed to be closed in a scissor-like pattern to form MOB from the late Carboniferous–Permian in the western segment, to Triassic–Jurassic in the central segment, and Cretaceous in the eastern segment (e.g., Zorin, 1999; Wang et al., 2022). Subduction-related arc magmatism, ranging from the Early Permian to the Late Triassic, has been identified on both sides of the MOB (e.g., Donskaya et al., 2013; Ganbat et al., 2021, 2022). In the central segment, southward subduction of the MOO plate initiated during the Late Carboniferous, as evidenced by a zircon U–Pb age of ~320 Ma from gabbros in the Adaatsag and Khukh Davaa ophiolitic complexes (Fig. 1b; Tomurtogoo et al., 2005; Zhu et al., 2018, 2023a), and the ocean finally closed in the Middle Jurassic at ~170 Ma (Tomurtogoo et al., 2005; Miao et al., 2017). In addition, Permian–Triassic arc magmatism is widespread along the southern flank of the MOB in its central segment (e.g., Zhao et al., 2017).

This study identifies magmatic events at ~220 Ma, ~192 Ma, and ~171 Ma, corresponding to arc, collisional, and post-collisional settings during the Late Triassic to Middle Jurassic (Fig. 10b). These magmatic episodes likely represent the late stages of the continuous southward subduction from the Permian to the Triassic and the eventual closure of the MOO in the central segment of the MOB (Fig. 11b).

In the eastern segment of the MOB, geochronological and tectonic evidence indicates continuous southward subduction of the MOO plate beneath the Erguna Massif from the Early Triassic to Middle Jurassic, with closure occurring in the Late Jurassic (e.g., Tang et al., 2016; Liu et al., 2018; Arzhannikova et al., 2022; Chen et al., 2024). This prolonged closure history is broadly consistent with the diachronous, scissor-like closure model of the MOO, suggesting progressive oceanic consumption from west to east, specifically from its central to eastern segment.

In the western segment of the MOB, multiple lines of evidence suggest that southward subduction of the MOO may have continued into the Late Triassic. Key examples include ~221 Ma adakitic rocks from the Luus area (Zhu et al., 2023c), ~220 Ma I-type granite in the Zambalkhudag area (Ganbat et al., 2021), and ~207 Ma bimodal volcanic rocks accompanied by coeval A-type granites in the Olzit area (Zhu et al., 2016). These magmatic suites have been interpreted as the result of arc- and back-arc extension-related magmatism associated with continued subduction processes during the Late Triassic. Although this interpretation remains controversial. For example, some studies suggest that the Late Triassic (~220–200 Ma) plutons in the western segment (e.g., Wang et al., 2022) represent post-accretionary stitching intrusions, implying that the closure of the MOO occurred before ~220 Ma, possibly during the Early Triassic. Field observations show that these plutons intrude the ~320 Ma Adaatsag ophiolite and its associated accretionary complexes, supporting their interpretation as post-accretionary intrusions. However, the Adaatsag ophiolite was formed in an intra-oceanic arc setting at ~320 Ma and was subsequently emplaced onto the continental margin before ~252 Ma, as a result of arc–continent collision (Zhu et al., 2023a). Notably, the ~220–200 Ma plutons in the western segment are characterized by slightly peraluminous, high-K calc-alkaline compositions and biotite ± hornblende mineral assemblages, exhibiting mineralogical and geochemical characteristics comparable to those of the arc-related Triassic granitoids analyzed in this study (Figs. 3–5; Table 1). Given this context, it is possible that the so-called post-accretionary (~220–200 Ma) granitoids in the western segment of the MOB intruded the ophiolitic sequences, which had already been emplaced onto the continental margin, during the continued southward subduction of the MOO in the Late Triassic.

Our results show that the MOO remained open in the central segment until the Early to Middle Jurassic, with subduction continuing in the eastern segment into the Late Jurassic. This pattern may support a revised scissor-like closure model progressing from the central to the eastern segments. In contrast, the timing of closure in the western segment remains uncertain. As discussed, some Late Triassic magmatic suites in that region may reflect continued subduction, although this interpretation remains debated. Taken together, the spatial and temporal variations across the belt suggest that MOO closure did not follow a simple west-to-east scissor-like sequence but instead involved a more complex, segment-specific history. This underscores the need to refine existing models by accounting for asynchronous and overlapping tectonic processes along the MOB.

7. Conclusion

This study identifies seven stages of magmatic activity in the Ereendavaa Block at ~880 Ma, ~540 Ma, ~470 Ma, ~440 Ma, ~220 Ma, ~190 Ma, and ~170 Ma. These stages likely correspond to major tectonic processes within the Central Asian Orogenic Belt, including the early breakup of Rodinia, the development of an active continental margin along the *peri*-Siberian realm, subsequent drift from this realm, and the eventual closure of the Mongol-Okhotsk Ocean. The spatial distribution of coeval magmatic and metamorphic events, from ~880 Ma to ~440 Ma, across other microcontinents within the Mongolian Collage suggests that the Ereendavaa Block evolved in tandem with neighboring microcontinents. This collective evolution likely began near the Siberian Craton earlier than ~880 Ma and continued until slightly later than ~440 Ma, when the Mongolian Collage may have drifted away from the Siberian Craton again. During the closure of the Mongol-Okhotsk Ocean, the Ereendavaa Block played a more pivotal role compared to other microcontinents within the Mongolian Collage. These findings underscore the Ereendavaa Block's crucial role in elucidating the evolution of the Paleo-Asian and Mongol-Okhotsk oceans, as well as the broader tectono-magmatic history of Mongolia and the central-eastern Central Asian Orogenic Belt.

CRediT authorship contribution statement

Munkhdelger Bold: Writing – original draft, Visualization, Investigation, Formal analysis. **Tatsuki Tsujimori:** Writing – review & editing, Supervision, Project administration, Methodology, Conceptualization. **Daniel Pastor-Galán:** Writing – review & editing, Writing – original draft, Visualization. **Tatsuro Adachi:** Writing – review & editing, Resources, Methodology, Investigation, Formal analysis. **Nobuhiko Nakano:** Writing – review & editing, Resources, Methodology, Investigation, Formal analysis. **Yasuhito Osanai:** Writing – review & editing, Supervision, Resources, Funding acquisition.

Declaration of competing interest

The authors declare that they have no known competing financial interests or personal relationships that could have appeared to influence the work reported in this paper. Co-author T. Tsujimori is an Associate Editor of this journal and was not involved in the editorial review or the decision to publish this article.

Acknowledgments

This research includes part of the first author's Master's thesis submitted to the Graduate School of Integrated Sciences for Global Society, Kyushu University. We extend our sincere gratitude to Jargalan Sereenen, Ippei Kitano, Otgonbayar Dandar, Dolzodmaa Boldbaatar, Ariuntsetseg Ganbat, Manzshir Bayrbold, Ryosuke Kato, Tamir Battogtokh, and Fransiska Ayuni Catur Wahyuandari for their invaluable support in manuscript preparation, laboratory analysis, and fieldwork. MB gratefully acknowledges the financial support provided by the JDS Scholarship and the Japanese Government MEXT Scholarship. DPG was funded by the grant KiTSuNE (PID2021-128801NA-I00) funded by 'MCIN/AEI/ESF Investing in Your Future', and a "Beca Leonardo" funded by the BBVA foundation. We are deeply grateful to Yongjiang Liu, the handling editor, and the two anonymous reviewers for their constructive comments and thoughtful suggestions, which significantly improved the quality of this manuscript.

Appendix A. Supplementary data

Supplementary data to this article can be found online at https://doi.org/10.1016/j.gr.2025.06.023.

References

Abdel-rahman, A.F.M., 1994. Nature of biotites from alkaline, calc-alkaline, and peraluminous magmas. J. Petrol. 35, 525–541. https://doi.org/10.1093/petrology/35.2.525.
Adachi, T., Kawakami, T., Higashino, F., Uno, M., 2023. Metamorphic rocks with different pressure–temperature–time paths bounded by a ductile shear zone at Oyayubi ridge, Brattnipene, Sør Rondane Mountains, East Antarctica. J. Mineral. Petrol. Sci. 118, 230220. https://doi.org/10.2465/JMPS.230220.
Adachi, T., Osanai, Y., Nakano, N., Owada, M., 2012. LA-ICP-MS U–Pb zircon and FE-EPMA U–Th–Pb monazite dating of pelitic granulites from the Mt. Ukidake area, Sefuri Mountains, northern Kyushu. J. Geol. Soc. Jpn 118, 39–52. https://doi.org/10.5575/geosoc.2011.0022.
Arzhannikova, A.V., Demonterova, E.I., Jolivet, M., Mikheeva, E.A., Ivanov, A.V., Arzhannikov, S.G., Khubanov, V.B., Kamenetsky, V.S., 2022. Segmental closure of the Mongol-Okhotsk Ocean: Insight from detrital geochronology in the East Transbaikalia Basin. Geosci. Front. 13, 101254. https://doi.org/10.1016/j.gsf.2021.101254.
Badarch, G., Dickson Cunningham, W., Windley, B.F., 2002. A new terrane subdivision for Mongolia: implications for the Phanerozoic crustal growth of Central Asia. J. Asian Earth Sci. 21, 87–110. https://doi.org/10.1016/S1367-9120(02)00017-2.
Barbarin, B., 1999. A review of the relationships between granitoid types, their origins and their geodynamic environments. Lithos 46, 605–626. https://doi.org/10.1016/S0024-4937(98)00085-1.
Bau, M., 1991. Rare-earth element mobility during hydrothermal and metamorphic fluid-rock interaction and the significance of the oxidation state of europium. Chem. Geol. 93, 219–230. https://doi.org/10.1016/0009-2541(91)90115-8.
Black, L.P., Kamo, S.L., Allen, C.M., Aleinikoff, J.N., Davis, D.W., Korsch, R.J., Foudoulis, C., 2003. TEMORA 1: a new zircon standard for phanerozoic U–Pb geochronology. Chem. Geol. 200, 155–170. https://doi.org/10.1016/S0009-2541(03)00165-7.
Blundy, J.D., Holland, T.J.B., 1990. Calcic amphibole equilibria and a new amphibole-plagioclase geothermometer. Contrib. Miner. Petrol. 104, 208–224. https://doi.org/10.1007/BF00306444.
Bold, U., Crowley, J.L., Smith, E.F., Sambuu, O., Macdonald, F.A., 2016a. Neoproterozoic to early Paleozoic tectonic evolution of the Zavkhan terrane of Mongolia: Implications for continental growth in the Central Asian orogenic belt. Lithosphere 8, 729–750. https://doi.org/10.1130/L549.1.
Bold, U., Isozaki, Y., Aoki, S., Sakata, S., Ishikawa, A., Sawaki, Y., Sawada, H., 2019. Precambrian basement, provenance implication, and tectonic evolution of the Gargan block of the Tuva-Mongolia terranes, Central Asian Orogenic Belt. Gondw. Res. 75, 172–183. https://doi.org/10.1016/j.gr.2019.05.003.
Bold, U., Smith, E.F., Rooney, A.D., Bowring, S.A., Buchwaldt, R., Dudás, F.O., Ramezani, J., Crowley, J.L., Schrag, D.P., Macdonald, F.A., 2016b. Neoproterozoic stratigraphy of the Zavkhan terrane of Mongolia: the backbone for Cryogenian and early Ediacaran chemostratigraphic records. Am. J. Sci. 316, 1–63. https://doi.org/10.2475/01.2016.01.
Bretshtein, Y.S., Klimova, A.V., 2007. Paleomagnetic study of late Proterozoic and Early Cambrian rocks in terranes of the Amur plate. Izvestiya. Phys. Solid Earth 43, 890–903. https://doi.org/10.1134/S1069351307100114.
Buriánek, D., Schulmann, K., Hrdličková, K., Hanžl, P., Janoušek, V., Gerdes, A., Lexa, O., 2017. Geochemical and geochronological constraints on distinct Early-Neoproterozoic and Cambrian accretionary events along southern margin of the Baydrag Continent in western Mongolia. Gondw. Res. 47, 200–227. https://doi.org/10.1016/j.gr.2016.09.008.
Buriánek, D., Soejono, I., Schulmann, K., Janoušek, V., Hanžl, P., Čáp, P., Bold, U., Svojtka, M., Collett, S., Žáček, V., 2022. Subduction-controlled temporal and spatial variations in early Palaeozoic sedimentary and volcanic record of the Mongol-Altai Domain. J. Asian Earth Sci. 230, 105182. https://doi.org/10.1016/j.jseaes.2022.105182.
Bussien, D., Gombojav, N., Winkler, W., von Quadt, A., 2011. The Mongol-Okhotsk Belt in Mongolia - an appraisal of the geodynamic development by the study of sandstone provenance and detrital zircons. Tectonophysics 510, 132–150. https://doi.org/10.1016/j.tecto.2011.06.024.
Cawood, P.A., 2005. Terra Australis Orogen: Rodinia breakup and development of the Pacific and Iapetus margins of Gondwana during the Neoproterozoic and Paleozoic. Earth Sci. Rev. 69, 249–279. https://doi.org/10.1016/j.earscirev.2004.09.001.
Cawood, P.A., Strachan, R.A., Pisarevsky, S.A., Gladkochub, D.P., Murphy, J.B., 2016. Linking collisional and accretionary orogens during Rodinia assembly and breakup: Implications for models of supercontinent cycles. Earth Planet. Sci. Lett. 449, 118–126. https://doi.org/10.1016/j.epsl.2016.05.049.
Chappell, B.W., 1996. Magma mixing and the production of compositional variation within granite suites: evidence from the granites of southeastern Australia. J. Petrol. 37, 449–470. https://doi.org/10.1093/petrology/37.3.449.
Chappell, B.W., Bryant, C.J., Wyborn, D., 2012. Peraluminous I-type granites. Lithos 153, 142–153. https://doi.org/10.1016/j.lithos.2012.07.008.
Chappell, B.W., White, A.J.R., 2001. Two contrasting granite types: 25 years later. Aust. J. Earth Sci. 48, 489–499. https://doi.org/10.1046/j.1440-0952.2001.00882.x.
Chen, L., Liang, C., Neubauer, F., Liu, Y., Yin, J., Gao, X., Zhao, J., 2024. Nature and multi-stage evolution of the Mongol-Okhotsk Ocean: New insights from the sedimentary record in the Mohe Basin. Earth Sci. Rev. 254, 104794. https://doi.org/10.1016/j.earscirev.2024.104794.
Clemens, J.D., Stevens, G., Farina, F., 2011. The enigmatic sources of I-type granites: the peritectic connexion. Lithos 126, 174–181. https://doi.org/10.1016/j.lithos.2011.07.004.
Cocks, L.R.M., Torsvik, T.H., 2007. Siberia, the wandering northern terrane, and its changing geography through the Palaeozoic. Earth Sci. Rev. 82, 29–74. https://doi.org/10.1016/j.earscirev.2007.02.001.
Collett, S., Soejono, I., Peřestý, V., Schulmann, K., Štípská, P., Míková, J., Novotná, N., 2024. Mongolian micro-continental blocks in Columbia/Nuna: Zircon U–Pb–Hf isotopic evidence for long-lasting Mongolia–Western Siberia connection. Terra Nova 36, 171–181. https://doi.org/10.1111/ter.12693.
Collins, W.J., Richards, S.W., 2008. Geodynamic significance of S-type granites in circum-Pacific orogens. Geology 36, 559–562. https://doi.org/10.1130/G24658A.1.
Crameri, F., Magni, V., Domeier, M., Shephard, G.E., Chotalia, K., Cooper, G., Eakin, C. M., Grima, A.G., Gürer, D., Király, Á., Mulyukova, E., Peters, K., Robert, B., Thielmann, M., 2020. A transdisciplinary and community-driven database to unravel subduction zone initiation. Nat. Commun. 11, 3750. https://doi.org/10.1038/s41467-020-17522-9.
Czamanske, G.K., Wones, D.R., 1973. Oxidation during magmatic differentiation, Finnmarka complex, Oslo area, Norway: Part 2, the mafic silicates1. J. Petrol. 14, 3750. https://doi.org/10.1093/petrology/14.3.349.
Daoudene, Y., Gapais, D., Ledru, P., Cocherie, A., Hocquet, S., Donskaya, T.V., 2009. The Ereendavaa Range (north-eastern Mongolia): an additional argument for Mesozoic extension throughout eastern Asia. Int. J. Earth Sci. 98, 1381–1393. https://doi.org/10.1007/s00531-008-0412-2.

Daoudene, Y., Ruffet, G., Cocherie, A., Ledru, P., Gapais, D., 2013. Timing of exhumation of the Ereendavaa metamorphic core complex (north-eastern Mongolia) – U–Pb and 40Ar/39Ar constraints. J. Asian Earth Sci. 62, 98–116. https://doi.org/10.1016/j.jseaes.2011.04.009.
Deer, W.A., Howie, R.A., Zussman, J., 1992. An Introduction to the Rock-Forming Minerals - Review, 2nd ed, Mineral. Mag.
Demoux, A., Kröner, A., Badarch, G., Jian, P., Tomurhuu, D., Wingate, M.T.D., 2009a. Zircon ages from the Baydrag block and the Bayankhongor ophiolite zone: Time constraints on late Neoproterozoic to Cambrian subduction- and accretion-related magmatism in central Mongolia. J. Geol. 117, 377–397. https://doi.org/10.1086/598947.
Demoux, A., Kröner, A., Liu, D., Badarch, G., 2009b. Precambrian crystalline basement in southern Mongolia as revealed by SHRIMP zircon dating. Int. J. Earth Sci. 98, 1365–1380. https://doi.org/10.1007/s00531-008-0321-4.
Domeier, M., Torsvik, T.H., 2014. Plate tectonics in the late Paleozoic. Geosci. Front. 5, 303–350. https://doi.org/10.1016/j.gsf.2014.01.002.
Donskaya, T.V., Gladkochub, D.P., 2021. Post-collisional magmatism of 1.88–1.84 Ga in the southern Siberian Craton: an overview. Precambr. Res. 367, 106447. https://doi.org/10.1016/j.precamres.2021.106447.
Donskaya, T. V., Gladkochub, D.P., Ernst, R.E., Pisarevsky, S.A., Mazukabzov, A.M., Demonterova, E.I., 2018. Geochemistry and petrogenesis of Mesoproterozoic dykes of the Irkutsk promontory, southern part of the Siberian Craton. Minerals 8, Article 545. doi: 10.3390/min8120545.
Donskaya, T.V., Gladkochub, D.P., Mazukabzov, A.M., Ivanov, A.V., 2013. Late Paleozoic - Mesozoic subduction-related magmatism at the southern margin of the Siberian continent and the 150 million-year history of the Mongol-Okhotsk Ocean. J. Asian Earth Sci. 62, 79–97. https://doi.org/10.1016/j.jseaes.2012.07.023.
Donskaya, T.V., Gladkochub, D.P., Mazukabzov, A.M., Wingate, M.T.D., 2014. Early Proterozoic postcollisional granitoids of the Biryusa block of the Siberian craton. Russ. Geol. Geophys. 55, 812–823. https://doi.org/10.1016/j.rgg.2014.06.002.
Donskaya, T.V., Sklyarov, E.V., Mazukabzov, A.M., 2000. Synkinematic intrusions of the framing of the Zagan metamorphic core complexes (southwestern Transbaikalia): Geochemistry and petrogenesis. Russ. Geol. Geophys. 41, 1320–1329.
Ernst, R.E., Wingate, M.T.D., Buchan, K.L., Li, Z.X., 2008. Global record of 1600-700 Ma Large Igneous Provinces (LIPs): Implications for the reconstruction of the proposed Nuna (Columbia) and Rodinia supercontinents. Precambr. Res. 160, 159–178. https://doi.org/10.1016/j.precamres.2007.04.019.
Eyal, M., Litvinovsky, B.A., Katzir, Y., Zanvilevich, A.N., 2004. The Pan-African high-K calc-alkaline peraluminous Elat granite from southern Israel: Geology, geochemistry and petrogenesis. J. Afr. Earth Sc. 40, 115–136. https://doi.org/10.1016/j.jafrearsci.2004.11.005.
Feng, Z., Liu, Y., Wu, P., Jin, W., Li, W., Wen, Q., Zhao, Y., Zhou, J., 2018. Silurian magmatism on the eastern margin of the Erguna Block, NE China: Evolution of the northern Great Xing'an Range. Gondw. Res. 61, 46–62. https://doi.org/10.1016/j.gr.2018.04.011.
Feng, Z., Zhang, Q., Liu, Y., Li, L., Jiang, L., Zhou, J., Li, W., Ma, Y., 2022. Reconstruction of Rodinia supercontinent: evidence from the Erguna Block (NE China) and adjacent units in the eastern Central Asian orogenic Belt. Precambr. Res. 368, 106467. https://doi.org/10.1016/J.PRECAMRES.2021.106467.
Frost, B.R., Barnes, C.G., Collins, W.J., Arculus, R.J., Ellis, D.J., Frost, C.D., 2001. A geochemical classification for granitic rocks. J. Petrol. 42, 2033–2048. https://doi.org/10.1093/petrology/42.11.2033.
Furnes, H., Safonova, I., 2019. Ophiolites of the Central Asian Orogenic Belt: Geochemical and petrological characterization and tectonic settings. Geosci. Front. 10, 1255–1284. https://doi.org/10.1016/j.gsf.2018.12.007.
Ganbat, A., Tsujimori, T., Miao, L., Safonova, I., Pastor-Galán, D., Anaad, C., Aoki, S., Aoki, K., Chimedsuren, M., 2022. Age, petrogenesis, and tectonic implications of the late Permian magmatic rocks in the Middle Gobi volcanoplutonic Belt, Mongolia. Island Arc 31, e12457. https://doi.org/10.1111/iar.12457.
Ganbat, A., Tsujimori, T., Miao, L., Safonova, I., Pastor-Galán, D., Anaad, C., Baatar, M., Aoki, S., Aoki, K., Savinskiy, I., 2021. Late Paleozoic–Early Mesozoic granitoids in the Khangay-Khentey basin, Central Mongolia: Implication for the tectonic evolution of the Mongol-Okhotsk Ocean margin. Lithos 404–405, 106455. https://doi.org/10.1016/j.lithos.2021.106455.
Gladkochub, D.P., Donskaya, T.V., Stanevich, A.M., Pisarevsky, S.A., Zhang, S., Motova, Z.L., Mazukabzov, A.M., Li, H., 2019. U–Pb detrital zircon geochronology and provenance of Neoproterozoic sedimentary rocks in southern Siberia: New insights into breakup of Rodinia and opening of Paleo-Asian Ocean. Gondw. Res. 65, 1–16. https://doi.org/10.1016/j.gr.2018.07.007.
Gladkochub, D.P., Donskaya, T.V., Wingate, M.T.D., Poller, U., Kröner, A., Fedorovsky, V.S., Mazukabzov, A.M., Todt, W., Pisarevsky, S.A., 2008. Petrology, geochronology, and tectonic implications of c. 500 Ma metamorphic and igneous rocks along the northern margin of the Central Asian Orogen (Olkhon terrane, Lake Baikal, Siberia). J. Geol. Soc. London 165, 235–246. https://doi.org/10.1144/0016-76492006-125.
Gladkochub, D.P., Pisarevsky, S.A., Donskaya, T.V., Ernst, R.E., Wingate, M.T.D., Söderlund, U., Mazukabzov, A.M., Sklyarov, E.V., Hamilton, M.A., Hanes, J.A., 2010. Proterozoic mafic magmatism in Siberian craton: an overview and implications for paleocontinental reconstruction. Precambr. Res. 183, 660–668. https://doi.org/10.1016/j.precamres.2010.02.023.
Glorie, S., De Grave, J., Buslov, M.M., Zhimulev, F.I., Safonova, I.Y., 2014. Detrital zircon provenance of early Palaeozoic sediments at the southwestern margin of the Siberian Craton: Insights from U–Pb geochronology. J. Asian Earth Sci. 82, 115–123. https://doi.org/10.1016/j.jseaes.2013.12.007.
Goodge, J.W., Vervoort, J.D., Fanning, C.M., Brecke, D.M., Farmer, G.L., Williams, I.S., Myrow, P.M., DePaolo, D.J., 2008. A positive test of East Antarctica-Laurentia juxtaposition within the Rodinia supercontinent. Science (1979) 321, 235–240. https://doi.org/10.1126/science.1159189.
Gou, J., Sun, D., Mao, A., Yang, D., Tang, Z., 2019. Geochronology and geochemistry of Ordovician plutons in the Erguna Block (NE China): further insights into the tectonic evolution of the Xing'an–Mongolia Orogenic Belt. Int. Geol. Rev. 61, 936–955. https://doi.org/10.1080/00206814.2018.1479890.
Gou, J., Sun, D.Y., Ren, Y.S., Liu, Y.J., Zhang, S.Y., Fu, C.L., Wang, T.H., Wu, P.F., Liu, X. M., 2013. Petrogenesis and geodynamic setting of Neoproterozoic and late Paleozoic magmatism in the Manzhouli-Erguna area of Inner Mongolia, China: Geochronological, geochemical and Hf isotopic evidence. J. Asian Earth Sci. 67–68, 114–137. https://doi.org/10.1016/j.jseaes.2013.02.016.
Halls, H.C., 2015. Paleomagnetic evidence for ∼4000 km of crustal shortening across the 1 Ga Grenville orogen of North America. Geology 43, 1051–1054. https://doi.org/10.1130/G37188.1.
Healy, B., Collins, W.J., Richards, S.W., 2004. A hybrid origin for Lachlan S-type granites: the Murrumbidgee Batholith example. Lithos 78, 197–216. https://doi.org/10.1016/j.lithos.2004.04.047.
Henry, D.J., Guidotti, C.V., Thomson, J.A., 2005. The Ti-saturation surface for low-to-medium pressure metapelitic biotites: Implications for geothermometry and Ti-substitution mechanisms. Am. Mineral. 90, 316–328. https://doi.org/10.2138/am.2005.1498.
Hoffman, P.F., 1991. Did the breakout of Laurentia turn Gondwanaland inside-out? Science 1979 (252), 1409–1412. https://doi.org/10.1126/science.252.5011.1409.
Hou, W., Zhao, G., Han, Y., Eizenhoefer, P.R., Zhang, X., Liu, Q., 2020. A ∼2.5 Ga magmatic arc in NE China: New geochronological and geochemical evidence from the Xinghuadukou complex. Geol. J. 55, 2550–2571. https://doi.org/10.1002/gj.3513.
Izokh, A.E., Vishnevskii, A.V., Polyakov, G.V., Shelepaev, R.A., 2011. Age of picrite and picrodolerite magmatism in western Mongolia. Russ. Geol. Geophys. 52, 7–23. https://doi.org/10.1016/j.rgg.2010.12.002.
Jahn, B.M., 2004. The central Asian orogenic belt and growth of the continental crust in the phanerozoic. Geol. Soc. Spec. Publ. 226, 73–100. https://doi.org/10.1144/GSL.SP.2004.226.01.05.
Jamyandorj, U., Tungalag, F., Boishenko, A.F., 1990. Geological map of the central and eastern Mongolia, scale 1:500,000. Institute of Geological Research Regional Geological Sector, Ministry of Heavy Industries (*in Mongolian*).
Janoušek, V., Jiang, Y., Buriánek, D., Schulmann, K., Hanžl, P., Soejono, I., Kröner, A., Altanbaatar, B., Erban, V., Lexa, O., Ganchuluun, T., Košler, J., 2018. Cambrian–Ordovician magmatism of the Ikh-Mongol Arc System exemplified by the Khantaishir Magmatic complex (Lake Zone, south–central Mongolia). Gondw. Res. 54, 122–149. https://doi.org/10.1016/j.gr.2017.10.003.
Jian, P., Kröner, A., Jahn, B., Windley, B.F., Shi, Y., Zhang, W., Zhang, F., Miao, L., Tomurhuu, D., Liu, D., 2014. Zircon dating of neoproterozoic and cambrian ophiolites in West Mongolia and implications for the timing of orogenic processes in the central part of the Central Asian Orogenic Belt. Earth Sci. Rev. 133, 62–93. https://doi.org/10.1016/j.earscirev.2014.02.006.
Jian, P., Kröner, A., Windley, B.F., Shi, Y., Zhang, F., Miao, L., Tomurhuu, D., Zhang, W., Liu, D., 2010. Zircon ages of the Bayankhongor ophiolite mélange and associated rocks: Time constraints on Neoproterozoic to Cambrian accretionary and collisional orogenesis in Central Mongolia. Precambr. Res. 177, 162–180. https://doi.org/10.1016/j.precamres.2009.11.009.
Jiang, Y.H., Zhao, P., Zhou, Q., Liao, S.Y., Jin, G.D., 2011. Petrogenesis and tectonic implications of early cretaceous S- and A-type granites in the northwest of the Gan-Hang rift, SE China. Lithos 121, 55–73. https://doi.org/10.1016/j.lithos.2010.10.001.
Kemp, A.I.S., Hawkesworth, C.J., Foster, G.L., Paterson, B.A., Woodhead, J.D., Hergt, J. M., Gray, C.M., Whitehouse, M.J., 2007. Magmatic and crustal differentiation history of granitic rocks from Hf-O isotopes in zircon. Science 1979 (315), 980–983. https://doi.org/10.1126/science.1136154.
Khain, E.V., Bibikova, E.V., Kröner, A., Zhuravlev, D.Z., Sklyarov, E.V., Fedotova, A.A., Kravchenko-Berezhnoy, I.R., 2002. The most ancient ophiolite of the Central Asian fold belt: U–Pb and Pb–Pb zircon ages for the Dunzhugur complex, Eastern Sayan, Siberia, and geodynamic implications. Earth Planet. Sci. Lett. 199, 311–325. https://doi.org/10.1016/S0012-821X(02)00587-3.
Khain, E.V., Bibikova, E.V., Salnikova, E.B., Kröner, A., Gibsher, A.S., Didenko, A.N., Degtyarev, K.E., Fedotova, A.A., 2003. The Palaeo-Asian ocean in the Neoproterozoic and early Palaeozoic: New geochronologic data and palaeotectonic reconstructions. Precambr. Res. 122, 329–358. https://doi.org/10.1016/S0301-9268(02)00218-8.
Kheraskova, T.N., Bush, V.A., Didenko, A.N., Samygin, S.G., 2010. Breakup of Rodinia and early stages of evolution of the Paleoasian ocean. Geotectonics 44, 3–24. https://doi.org/10.1134/S0016852110010024.
Kilian, T.M., Swanson-Hysell, N.L., Bold, U., Crowley, J., Macdonald, F.A., 2016. Paleomagnetism of the Teel basalts from the Zavkhan terrane: Implications for Paleozoic paleogeography in Mongolia and the growth of continental crust. Lithosphere 8, 699–715. https://doi.org/10.1130/L552.1.
Kitano, I., Osanai, Y., Nakano, N., Adachi, T., Yoshimoto, A., 2014. Rapid techniques for zircon separation and the application for U–Pb dating. Bull. Grad. Sch. Soc. Cult. Stud., Kyushu Univ. 20, 1–10 in Japanese with English abstract.
Kovach, V., Kozakov, I., Kröner, A., Salnikova, E., Wang, K.L., Lee, H.Y., Plotkina, J., Gorokhovsky, B., Adamskaya, E., Tolmacheva, E., Shpakovich, L., 2021. Early neoproterozoic crustal growth and microcontinent formation of the north–central Central Asian Orogenic Belt: New geological, geochronological, and Nd–Hf isotopic data on the Mélange Zone within the Zavkhan terrane, western Mongolia. Gondw. Res. 91, 254–276. https://doi.org/10.1016/j.gr.2020.12.022.

Kovach, V.P., Kozakov, I.K., Wang, K.L., Plotkina, Y.V., Lee, H.Y., Chung, S.L., 2019. Age and sources of terrigenous rocks of basal formation of the Tsagaan-Olom Group of the Dzabkhan Terrane: results of U–Th–Pb Geochronological, Lu–Hf and Sm–Nd isotopic studies. Stratigraphy and Geol. Correl. 27, 555–572. https://doi.org/10.1134/S0869593819050046.

Kovalenko, D.V., Mongush, A.A., Ageeva, O.A., Eenzhin, G., 2014. Sources and geodynamic environments of formation of Vendian-Early Paleozoic magmatic complexes in the Daribi range, Western Mongolia. Petrology 22, 389–417. https://doi.org/10.1134/S0869591114040043.

Kozakov, I.K., Kovach, V.P., Bibikova, E.V., Kirnozova, T.I., Lykhin, D.A., Plotkina, Y.V., Tolmacheva, E.V., Fugzan, M.M., Erdenezhargal, C., 2014. Late Riphean episode in the formation of crystalline rock complexes in the Dzabkhan microcontinent: Geological, geochronologic, and Nd isotopic-geochemical data. Petrology 22, 480–506. https://doi.org/10.1134/S086959111405004X.

Kozakov, I.K., Kozlovsky, A.M., Yarmolyuk, V.V., Kovach, V.P., Bibikova, E.V., Kirnozova, T.I., Plotkina, Y.V., Zagornaya, N.Y., Fugzan, M.M., Erdenejargal, C., Lebedev, V.I., Eenjin, G., 2011. Crystalline complexes of the Tarbagatai block of the Early Caledonian superterrane of Central Asia. Petrology 19, 426–444. https://doi.org/10.1134/S0869591111040047.

Kozakov, I.K., Kuznetsov, A.B., Erdenegargal, C., Salnikova, E.B., Anisimova, I.V., Plotkina, J.V., Fedoseenko, A.M., 2017. Neoproterozoic complexes of the shelf cover of the Dzabkhan terrane basement in the Central Asian Orogenic Belt. Stratigr. Geol. Correl. 25, 479–491. https://doi.org/10.1134/S0869593817050045.

Kozakov, I.K., Sal'nikova, E.B., Wang, T., Didenko, A.N., Plotkina, Y.V., Podkovyrov, V. N., 2007. Early precambrian crystalline complexes of the central Asian microcontinent: Age, sources, tectonic position. Stratigr. Geol. Correl. 15, 121–140. https://doi.org/10.1134/S0869593807020013.

Kozakov, I.K., Yarmolyuk, V.V., Kovach, V.P., Bibikova, E.V., Kirnozova, T.I., Kozlovskii, A.M., Plotkina, Y.V., Fugzan, M.M., Lebedev, V.I., Erdenezhargal, C., 2012. The Early Baikalian crystalline complex in the basement of the Dzabkhan microcontinent of the Early Caledonian orogenic area, Central Asia. Stratigr. Geol. Correl. 20, 231–239. https://doi.org/10.1134/S0869593812030057.

Kravchinsky, V.A., Sklyarov, E.V., Gladkochub, D.P., Harbert, W.P., 2010. Paleomagnetism of the Precambrian Eastern Sayan rocks: Implications for the Ediacaran-Early Cambrian paleogeography of the Tuva-Mongolian composite terrane. Tectonophysics 486, 65–80. https://doi.org/10.1016/j.tecto.2010.02.010.

Kröner, A., Kovach, V.P., Kozakov, I.K., Kirnozova, T., Azimov, P., Wong, J., Geng, H.Y., 2015. Zircon ages and Nd-Hf isotopes in UHT granulites of the Ider complex: a cratonic terrane within the Central Asian Orogenic Belt in NW Mongolia. Gondw. Res. 27, 1392–1406. https://doi.org/10.1016/j.gr.2014.03.005.

Kröner, A., Lehmann, J., Schulmann, K., Demoux, A., Lexa, O., Tomurhuu, D., Štípská, P., Liu, D., Wingat, M.T.D., 2010. Lithostratigraphic and geochronological constraints on the evolution of the central asian orogenic belt in SW Mongolia: Early Paleozoic rifting followed by late Paleozoic accretion. Am. J. Sci. 310, 523–574. https://doi.org/10.2475/07.2010.01.

Kröner, A., Windley, B.F., Badarch, G., Tomurtogoo, O., Hegner, E., Jahn, B.M., Gruschka, S., Khain, E.V., Demoux, A., Wingate, M.T.D., 2007. Accretionary growth and crust formation in the Central Asian Orogenic Belt and comparison with the Arabian-Nubian shield. Geol. Soc. Am. Mem. 200, 181–209. https://doi.org/10.1130/2007.1200(11).

Kurihara, T., Tsukada, K., Otoh, S., Kashiwagi, K., Chuluun, M., Byambadash, D., Boijir, B., Gonchigdorj, S., Nuramkhan, M., Niwa, M., Tokiwa, T., Hikichi, G., Kozuka, T., 2009. Upper Silurian and Devonian pelagic deep-water radiolarian chert from the Khangai-Khentei belt of Central Mongolia: evidence for Middle Paleozoic subduction-accretion activity in the Central Asian Orogenic Belt. J. Asian Earth Sci. 34, 209–225. https://doi.org/10.1016/j.jseaes.2008.04.010.

Kurimoto, C., Tungalag, F., Bayarmandal, L., Ichinnorov, N., 1998. K-Ar ages of white mica from pelitic schists of the Bayankhongor area, west Mongolia. Bull. Geol. Surv. Jpn 49, 19–23.

Kuzmichev, A.B., Bibikova, E.V., Zhuravlev, D.Z., 2001. Neoproterozoic (~ 800 Ma) orogeny in the Tuva-Mongolia Massif (Siberia): Island arc-continent collision at the northeast Rodinia margin. Precambr. Res. 110, 109–126. https://doi.org/10.1016/S0301-9268(01)00183-8.

Kuzmichev, A.B., Larionov, A.N., 2013. Neoproterozoic island arcs in East Sayan: Duration of magmatism (from U–Pb zircon dating of volcanic clastics). Russ. Geol. Geophys. 54, 34–43. https://doi.org/10.1016/j.rgg.2012.12.003.

Lamont, T.N., Roberts, N.M.W., Searle, M.P., Gardiner, N.J., Gopon, P., Hsieh, Y.T., Holdship, P., White, R.W., 2023. Contemporaneous crust-derived I- and S-type granite magmatism and normal faulting on Tinos, Delos, and Naxos, Greece: Constraints on Aegean orogenic collapse. Bull. Geol. Soc. Am. 135, 2797–2829. https://doi.org/10.1130/B36489.1.

Leake, B.E., Woolley, A.R., Arps, C.E.S., Birch, W.D., Gilbert, M.C., Grice, J.D., Hawthorne, F.C., Kato, A., Kisch, H.J., Krivovichev, V.G., Linthout, K., Laird, J., Mandarino, J.A., Maresch, W.V., Nickel, E.H., Rock, N.M.S., Schumacher, J.C., Smith, D.C., Stephenson, N.C.N., Ungaretti, L., Whittaker, E.J.W., Youzhi, G., 1997. Nomenclature of amphiboles: Report of the subcommittee on amphiboles of the international mineralogical association, commission on new minerals and mineral names. Am. Mineral. 82, 295–310. https://doi.org/10.1180/minmag.1997.061.405.13.

Levashova, N.M., Kalugin, V.M., Gibsher, A.S., Yff, J., Ryabinin, A.B., Meert, J.G., Malone, S.J., 2010. The origin of the Baydaric microcontinent, Mongolia: Constraints from paleomagnetism and geochronology. Tectonophysics 485, 306–320. https://doi.org/10.1016/j.tecto.2010.01.012.

Levashova, N.M., Meert, J.G., Gibsher, A.S., Grice, W.C., Bazhenov, M.L., 2011. The origin of microcontinents in the Central Asian Orogenic Belt: Constraints from paleomagnetism and geochronology. Precambr. Res. 185, 37–54. https://doi.org/10.1016/j.precamres.2010.12.001.

Li, X., Zhang, C., 2022. Machine learning thermobarometry for biotite-bearing magmas. J. Geophys. Res. Solid Earth 127. https://doi.org/10.1029/2022JB024137.

Li, Z.X., Bogdanova, S.V., Collins, A.S., Davidson, A., De Waele, B., Ernst, R.E., Fitzsimons, I.C.W., Fuck, R.A., Gladkochub, D.P., Jacobs, J., Karlstrom, K.E., Lu, S., Natapov, L.M., Pease, V., Pisarevsky, S.A., Thrane, K., Vernikovsky, V., 2008. Assembly, configuration, and break-up history of Rodinia: a synthesis. Precambr. Res. 160, 179–210. https://doi.org/10.1016/j.precamres.2007.04.021.

Li, Z.Y., Jiang, Y.D., Collett, S., Štípská, P., Schulmann, K., Wang, S., Sukhorukov, V., Bai, X.J., Zhang, W.F., 2023. Peri-Siberian ordovician to devonian tectonic switching in the Olkhon Terrane (Southern Siberia): structural and geochronological constraints. e2023TC007826 Tectonics 42. https://doi.org/10.1029/2023TC007826.

Likhanov, I.I., 2022. Provenance, age, and tectonic settings of rock complexes (Transangarian Yenisey Ridge, East Siberia): geochemical and geochronological evidence. Geosciences 11, 402. https://doi.org/10.3390/geosciences12110402.

Likhanov, I.I., Nozhkin, A.D., Reverdatto, V.V., Kozlov, P.S., 2014. Grenville tectonic events and evolution of the Yenisei Ridge at the western margin of the Siberian Craton. Geotectonics 48, 371–389. https://doi.org/10.1134/S0016852114050045.

Likhanov, I.I., Popov, N.V., Nozhkin, A.D., 2012. The oldest granitoids in the Transangarian part of the Yenisey Ridge: U–Pb and Sm–Nd data and geodynamic settings. Geochem. Int. 50, 869–877. https://doi.org/10.1134/S0016702912080058.

Likhanov, I.I., Reverdatto, V.V., 2015. Evidence of Middle Neoproterozoic extensional tectonic settings along the western margin of the Siberian craton: Implications for the breakup of Rodinia. Geochem. Int. 53, 671–689. https://doi.org/10.1134/S0016702915080030.

Likhanov, I.I., Reverdatto, V.V., Kozlov, P.S., Khiller, V.V., Sukhorukov, V.P., 2015. P-T-t constraints on polymetamorphic complexes of the Yenisey Ridge, East Siberia: Implications for Neoproterozoic paleocontinental reconstructions. J. Asian Earth Sci. 113, 391–410. https://doi.org/10.1016/j.jseaes.2014.10.026.

Likhanov, I.I., Reverdatto, V.V., Kozlov, P.S., Savko, K.A., Krylov, A.A., 2022. Petrogenesis, U–Pb Age, and Lu–Hf systematics of rocks of the Garevka complex (Northern Yenisei Ridge): evidence of the Grenville events at the Western Margin of the Siberian Craton. Dokl. Earth Sci. 507, 1071–1079. https://doi.org/10.1134/S1028334X22600815.

Liu, H., Li, Y., He, H., Huangfu, P., Liu, Y., 2018. Two-phase southward subduction of the Mongol-Okhotsk oceanic plate constrained by Permian-Jurassic granitoids in the Erguna and Xing'an massifs (NE China). Lithos 304–307, 347–361. https://doi.org/10.1016/j.lithos.2018.01.016.

Liu, H., Li, Y., Wan, Z., Lai, C.K., 2020. Early neoproterozoic tectonic evolution of the Erguna Terrane (NE China) and its paleogeographic location in Rodinia supercontinent: Insights from magmatic and sedimentary record. Gondw. Res. 88, 185–200. https://doi.org/10.1016/j.gr.2020.07.005.

Liu, Y., Li, W., Ma, Y., Feng, Z., Guan, Q., Li, S., Chen, Z., Liang, C., Wen, Q., 2021. An orocline in the eastern Central Asian Orogenic Belt. Earth Sci. Rev. 221, 103808. https://doi.org/10.1016/j.earscirev.2021.103808.

Liu, Y., Xiao, W., Ma, Y., Li, S., Peskov, A.Y., Chen, Z., Zhou, T., Guan, Q., 2023. Oroclines in the central asian orogenic belt. Natl. Sci. Rev. 10, nwac243. https://doi.org/10.1093/nsr/nwac243.

Lu, S., Zhao, G., Wang, H., Hao, G., 2008. Precambrian metamorphic basement and sedimentary cover of the North China Craton: a review. Precambr. Res. 160, 77–93. https://doi.org/10.1016/j.precamres.2007.04.017.

Ludwig, K.R., 2008. User's Manual for Isoplot 3.70. Berkeley Geochronol. Center Spec. Publ. 76.

Luo, B., Liu, R., Zhang, H., Zhao, J., Yang, H., Xu, W., Guo, L., Zhang, L., Tao, L., Pan, F., Wang, W., Gao, Z., Shao, H., 2018. Neoproterozoic continental back-arc rift development in the Northwestern Yangtze Block: evidence from the Hannan intrusive magmatism. Gondw. Res. 59, 27–42. https://doi.org/10.1016/j.gr.2018.03.012.

Maniar, P.D., Piccoli, P.M., 1989. Tectonic discrimination of granitoids. Geol. Soc. Am. Bull. 101, 635–643. https://doi.org/10.1130/0016-7606(1989)101<0635:TDOG>2.3.CO;2.

Meert, J.G., Santosh, M., 2017. The Columbia supercontinent revisited. Gondw. Res. 50, 67–83. https://doi.org/10.1016/j.gr.2017.04.011.

Merdith, A.S., Collins, A.S., Williams, S.E., Pisarevsky, S., Foden, J.D., Archibald, D.B., Blades, M.L., Alessio, B.L., Armistead, S., Plavsa, D., Clark, C., Müller, R.D., 2017. A full-plate global reconstruction of the Neoproterozoic. Gondw. Res. 50, 84–134. https://doi.org/10.1016/j.gr.2017.04.001.

Miao, L., Baatar, M., Zhang, F., Anaad, C., Zhu, M., Yang, S., 2016. Cambrian Kherlen ophiolite in northeastern Mongolia and its tectonic implications: SHRIMP zircon dating and geochemical constraints. Lithos 261, 128–143. https://doi.org/10.1016/j.lithos.2015.12.012.

Miao, L., Zhang, F., Baatar, M., Zhu, M., Anaad, C., 2017. SHRIMP zircon U–Pb ages and tectonic implications of igneous events in the Ereendavaa metamorphic terrane in NE Mongolia. J. Asian Earth Sci. 144, 243–260. https://doi.org/10.1016/j.jseaes.2017.03.005.

McLennan, S.M., 1989. Chapter 7: Rare Earth Elements in Sedimentary Rocks: Influence of Provenance and Sedimentary Processes. R.L. Bruce, G.A. McKay (Eds.), Geochemistry and Mineralogy of Rare Earth Elements, De Gruyter, Berlin, Boston (1989), 169–200. doi: 10.1515/9781501509032-010.

Miao, L., Zhu, M., Liu, C., Baatar, M., Anaad, C., Yang, S., Li, X., 2020. Detrital-zircon age spectra of Neoproterozoic-Paleozoic sedimentary rocks from the Ereendavaa terrane in NE Mongolia: Implications for the early-stage evolution of the Ereendavaa terrane

and the Mongol-Okhotsk Ocean. Minerals 10, Article 742. doi: 10.3390/MIN10090742.
Middlemost, E.A.K., 1994. Naming materials in the magma/igneous rock system. Earth Sci. Rev. 37, 215–224. https://doi.org/10.1016/0012-8252(94)90029-9.
Molina, J.F., Scarrow, J.H., Montero, P.G., Bea, F., 2009. High-Ti amphibole as a petrgenetic indicator of magma chemistry: evidence for mildly alkalic-hybrid melts during evolution of Variscan basic-ultrabasic magmatism of Central Iberia. Contrib. Miner. Petrol. 158, 69–98. https://doi.org/10.1007/s00410-008-0371-4.
Moyen, J.F., Laurent, O., Chelle-Michou, C., Couzinié, S., Vanderhaeghe, O., Zeh, A., Villaros, A., Gardien, V., 2017. Collision vs. subduction-related magmatism: two contrasting ways of granite formation and implications for crustal growth. Lithos 277, 154–177. https://doi.org/10.1016/j.lithos.2016.09.018.
Mutch, E.J.F., Blundy, J.D., Tattitch, B.C., Cooper, F.J., Brooker, R.A., 2016. An experimental study of amphibole stability in low-pressure granitic magmas and a revised Al-in-hornblende geobarometer. Contrib. Miner. Petrol. 171, 85. https://doi.org/10.1007/s00410-016-1298-9.
Nachit, H., Ibhi, A., Abia, E.H., Ben Ohoud, M., 2005. Discrimination between primary magmatic biotites, reequilibrated biotites and neoformed biotites. Comptes Rendus. Géoscience 337, 1415–1420. https://doi.org/10.1016/j.crte.2005.09.002.
Nachit, H., Razafimahefa, N., Stussi, J.M., Carron, J.P., 1985. Composition chimique des biotites et typologie magmatique des granitoides. Comptes Rendus De L'academie Des Sciences, Paris, Serie II 301, 813–818.
Nakano, N., Osanai, Y., Adachi, T., Yonemura, K., Yoshimoto, A., Setiawan, N., 2012. Rapid techniques for quantitative determination of major, trace and rare earth elements in low dilution glass bead using XRF and LA-ICP-MS. Bull. Grad. Sch. Soc. Cult. Stud., Kyushu University 18, 81–94. https://doi.org/10.15017/21861.
Narantsetseg, T., Chao, Y., Tao, W., Zhongyuan, R., Pengfei, L., Le, Z., Lei, G., Ying, T., Orolmaa, D., Battushig, A., Baatarchuluun, O., Idermunkh, T., Tumendelger, J., 2021. Metamorphic rocks from the north-eastern part of the Ereendavaa terrane (Eastern Mongolia): an origin of the Permian back-arc basin rather than the Proterozoic basement. Mong. Geosci. 26, 16–45. https://doi.org/10.5564/mgs.v26i52.1079.
Narantsetseg, T., Orolmaa, D., Yuan, C., Wang, T., Guo, L., Tong, Y., Wang, X., Enkh-Orshikh, O., Oyunchimeg, T.U., Delgerzaya, P., Enkhdalai, B., 2019. Early-Middle Paleozoic volcanic rocks from the Ereendavaa terrane (Tsarigiin gol area, NE Mongolia) with implications for tectonic evolution of the Kherlen massif. J. Asian Earth Sci. 175, 138–157. https://doi.org/10.1016/j.jseaes.2018.12.008.
Nicolosi, I., Speranza, F., Chiappini, M., 2006. Ultrafast oceanic spreading of the Marsili Basin, southern Tyrrhenian Sea: evidence from magnetic anomaly analysis. Geology 34, 717–720. https://doi.org/10.1130/G22555.1.
Nozhkin, A.D., Borisenko, A.S., Nevol'ko, P.A., 2011. Stages of late Proterozoic magmatism and periods of Au mineralization in the Yenisei Ridge. Russ. Geol. Geophys. 52, 124–143. https://doi.org/10.1016/j.rgg.2010.12.010.
Nozhkin, A.D., Popov, N.V., Dmitrieva, N.V., Storozhenko, A.A., Vasil'ev, N.F., 2015. Neoproterozoic collisional S-type granitoids of the Yenisei Ridge: Petrogeochemical composition and U–Pb, Ar–Ar, and Sm–Nd isotope data. Russ. Geol. Geophys. 56, 689–695. https://doi.org/10.1016/j.rgg.2015.04.001.
Nozhkin, A.D., Turkina, O.M., Likhanov, I.I., 2023. Neoproterozoic Collision Granitoids in the Southwestern Margin of the Siberian Craton: Chemical Composition, U−Pb Age, and Formation Conditions of the Gusyanka Massif. Geochem. Int. 61, 484–498. https://doi.org/10.1134/S0016702923050063.
Orolmaa, D., Turbold, S., Odgerel, D., 2015. Lower Paleozoic granitoids of Undurkhaan district: geochronology and geochemistry. Explorer 53, 54–68 in Mongolian.
Otten, M.T., 1984. The origin of brown hornblende in the Artfjället gabbro and dolerites. Contrib. Miner. Petrol. 86, 189–199. https://doi.org/10.1007/BF00381846.
Paces, J.B., Miller, J.D., 1993. Precise U–Pb ages of Duluth complex and related mafic intrusions, northeastern Minnesota: geochronological insights to physical, petrogenetic, paleomagnetic, and tectonomagmatic processes associated with the 1.1 Ga Midcontinent Rift system. J. Geophys. Res. 98, 13997–14013. https://doi.org/10.1029/93jb01159.
Pál-Molnár, E., Batki, A., Ódri, Á., Kiss, B., Almási, E., 2015. Geochemical implications for the magma origin of granitic rocks from the Ditrău Alkaline Massif (Eastern Carpathians, Romania). Geologia Croatica 68, 51–66. https://doi.org/10.4154/gc.2015.04.
Pastor-Galán, D., 2022. From supercontinent to superplate: late Paleozoic Pangea's inner deformation suggests it was a short-lived superplate. Earth Sci. Rev. 226, 103918. https://doi.org/10.1016/j.earscirev.2022.103918.
Pastor-Galán, D., Nance, R.D., Murphy, J.B., Spencer, C.J., 2019. Supercontinents: Myths, mysteries, and milestones. Geol. Soc. Spec. Publ. 470, 39–64. https://doi.org/10.1144/SP470.16.
Patiño Douce, A.E., 1999. What do experiments tell us about the relative contributions of crust and mantle to the origin of granitic magmas? Geol. Soc. Spec. Publ. 168, 55–75. https://doi.org/10.1144/GSL.SP.1999.168.01.05.
Pearce, J.A., Harris, N.B.W., Tindle, A.G., 1984. Trace element discrimination diagrams for the tectonic interpretation of granitic rocks. J. Petrol. 25, 956–983. https://doi.org/10.1093/petrology/25.4.956.
Peccerillo, A., Taylor, S.R., 1976. Geochemistry of Eocene calc-alkaline volcanic rocks from the Kastamonu area, Northern Turkey. Contrib. Miner. Petrol. 58, 63–81. https://doi.org/10.1007/BF00384745.
Petrik, I., Broska, I., Uher, P., 1994. Evolution of the western Carpathian granite magmatism: age, source rock, geotectonic setting and relation to the Variscan structure. Geol. Carpath. 45, 283–291.
Pfander, J.A., Jochum, K.P., Kozakov, I., Kroner, A., Todt, W., 2002. Coupled evolution of back-arc and island arc-like mafic crust in the late-Neoproterozoic Agardagh Tes-Chem ophiolite, Central Asia: evidence from trace element and Sr-Nd-Pb isotope data. Contrib. Miner. Petrol. 143, 154–174. https://doi.org/10.1007/s00410-001-0340-7.
Pisarevsky, S.A., Natapov, L.M., 2003. Siberia and Rodinia. Tectonophysics 375, 221–245. https://doi.org/10.1016/j.tecto.2003.06.001.
Pisarevsky, S.A., Natapov, L.M., Donskaya, T.V., Gladkochub, D.P., Vernikovsky, V.A., 2008. Proterozoic Siberia: a promontory of Rodinia. Precambr. Res. 160, 66–76. https://doi.org/10.1016/j.precamres.2007.04.016.
Popov, N.V., Likhanov, I.I., Nozhkin, A.D., 2010. Mesoproterozoic granitoid magmatism in the Trans-Angara segment of the Yenisei Range: U–Pb evidence. Dokl. Earth Sci. 431, 418–423. https://doi.org/10.1134/S1028334X10040021.
Priyatkina, N., Collins, W.J., Khudoley, A.K., Letnikova, E.F., Huang, H.Q., 2018. The Neoproterozoic evolution of the western Siberian Craton margin: U–Pb–Hf isotopic records of detrital zircons from the Yenisey Ridge and the Prisayan Uplift. Precambr. Res. 305, 197–217. https://doi.org/10.1016/j.precamres.2017.12.014.
Ridolfi, F., Renzulli, A., 2012. Calcic amphiboles in calc-alkaline and alkaline magmas: Thermobarometric and chemometric empirical equations valid up to 1,130°C and 2.2 GPa. Contrib. Miner. Petrol. 163, 877–895. https://doi.org/10.1007/s00410-011-0704-6.
Ridolfi, F., Renzulli, A., Puerini, M., 2010. Stability and chemical equilibrium of amphibole in calc-alkaline magmas: an overview, new thermobarometric formulations and application to subduction-related volcanoes. Contrib. Miner. Petrol. 160, 45–66. https://doi.org/10.1007/s00410-009-0465-7.
Rudnev, S.N., Izokh, A.E., Borisenko, A.S., Shelepaev, R.A., Orihashi, Y., Lobanov, K.V., Vishnevsky, A.V., 2012. Early Paleozoic magmatism in the Bumbat-Hairhan area of the Lake Zone in western Mongolia (geological, petrochemical, and geochronological data). Russ. Geol. Geophys. 53, 425–441. https://doi.org/10.1016/j.rgg.2012.03.004.
Rudnev, S.N., Izokh, A.E., Kovach, V.P., Shelepaev, R.A., Terent'eva, L.B., 2009. Age, composition, sources, and geodynamic environments of the origin of granitoids in the northern part of the Ozernaya zone, western Mongolia: Growth mechanisms of the Paleozoic continental crust. Petrology 17, 439–475. https://doi.org/10.1134/S0869591109050026.
Rudnev, S.N., Kovach, V.P., Ponomarchuk, V.A., 2013. Vendian-Early Cambrian island-arc plagiogranitoid magmatism in the Altai-Sayan folded area and in the Lake Zone of western Mongolia (geochronological, geochemical, and isotope data). Russ. Geol. Geophys. 54, 1272–1287. https://doi.org/10.1016/j.rgg.2013.09.010.
Safonova, I., 2017. Juvenile versus recycled crust in the Central Asian Orogenic Belt: Implications from ocean plate stratigraphy, blueschist belts and intra-oceanic arcs. Gondw. Res. 47, 6–27. https://doi.org/10.1016/j.gr.2016.09.003.
Safonova, I., Kotlyarov, A., Krivonogov, S., Xiao, W., 2017. Intra-oceanic arcs of the Paleo-Asian Ocean. Gondw. Res. 50, 167–194. https://doi.org/10.1016/j.gr.2017.04.005.
Safonova, I., Maruyama, S., 2014. Asia: a frontier for a future supercontinent Amasia. Int. Geol. Rev. 56, 1051–1071. https://doi.org/10.1080/00206814.2014.915586.
Schmidt, M.W., 1992. Amphibole composition in tonalite as a function of pressure: an experimental calibration of the Al-in-hornblende barometer. Contrib. Miner. Petrol. 110, 304–310. https://doi.org/10.1007/BF00310745.
Şengör, A.M.C., Natal'In, B.A., Burtman, V.S., 1993. Evolution of the Altaid tectonic collage and Palaeozoic crustal growth in Eurasia. Nature 364, 299–307. https://doi.org/10.1038/364299a0.
Sergelen, U., 2018. Geochronology of assumed cratonal terranes in Mongolia. Kyushu University, Fukuoka. Unpublished master's thesis.
Sheldrick, T.C., Barry, T.L., Millar, I.L., Barfod, D.N., Halton, A.M., Smith, D.J., 2020. Evidence for southward subduction of the Mongol-Okhotsk oceanic plate: Implications from Mesozoic adakitic lavas from Mongolia. Gondw. Res. 79, 140–156. https://doi.org/10.1016/j.gr.2019.09.007.
Sisson, T.W., Grove, T.L., Coleman, D.S., 1996. Hornblende gabbro sill complex at Onion Valley, California, and a mixing origin for the Sierra Nevada batholith. Contrib. Miner. Petrol. 126, 81–108. https://doi.org/10.1007/s004100050237.
Skuzovatov, S., 2021. Nature and (in-)coherent metamorphic evolution of subducted continental crust in the Neoproterozoic accretionary collage of SW Mongolia. Geosci. Front. 12, 101097. https://doi.org/10.1016/j.gsf.2020.10.004.
Soejono, I., Collett, S., Schulmann, K., Štípská, P., Míková, J., Peřestý, V., Novotná, N., Guy, A., 2025. Neoproterozoic paleogeography and displacement of the Mongolian blocks constrained by detrital zircon ages and Hf isotopic systematics (Zavkhan Block, W Mongolia). Precambr. Res. 417, 107657. https://doi.org/10.1016/j.precamres.2024.107657.
Soejono, I., Janoušek, V., Peřestý, V., Schulmann, K., Svojtka, M., Hanžl, P., Hora, J.M., Míková, J., Štípská, P., Guy, A., Collett, S., Otgonbaatar, D., 2023. From Rodinian passive margin to peri-Siberian continental arc: evidence from the multiphase Neoproterozoic–early Paleozoic magmatic record of the Zavkhan Block in the Mongolian Collage. Gondw. Res. 121, 344–367. https://doi.org/10.1016/j.gr.2023.05.001.
Soejono, I., Peřestý, V., Schulmann, K., Čopjaková, R., Svojtka, M., Štípská, P., Buriánek, D., Janoušek, V., Lexa, O., 2021. Structural, metamorphic and geochronological constraints on Palaeozoic multi-stage geodynamic evolution of the Altai accretionary wedge system (Hovd Zone, western Mongolia). Lithos 396–397, 106204. https://doi.org/10.1016/j.lithos.2021.106204.
Soret, M., Bonnet, G., Agard, P., Larson, K.P., Cottle, J.M., Dubacq, B., Kylander-Clark, A. R.C., Button, M., Rividi, N., 2022. Timescales of subduction initiation and evolution of subduction thermal regimes. Earth Planet. Sci. Lett. 584, 117521. https://doi.org/10.1016/j.epsl.2022.117521.
Sorokin, A.A., Kudryashov, N.M., Kotov, A.B., Kovach, V.P., 2017. Age and tectonic setting of the early Paleozoic magmatism of the Mamyn Terrane, Central Asian Orogenic Belt, Russia. J. Asian Earth Sci. 144, 22–39. https://doi.org/10.1016/j.jseaes.2017.01.017.

Stern, R.J., Gerya, T., 2018. Subduction initiation in nature and models: a review. Tectonophysics 746, 173–198. https://doi.org/10.1016/j.tecto.2017.10.014.

Štípská, P., Peřestý, V., Soejono, I., Schulmann, K., Kylander-Clark, R.C.A., Aguilar, C., Collett, S., Racek, M., Míková, J., Dorjsuren, O., Novotná, N., 2023. Anticlockwise metamorphic paths at ca. 890–790 Ma from the NE Baidrag block, Mongolia, indicate back-arc compression at the Rodinia periphery. Geosci. Front. 14, 101520. https://doi.org/10.1016/j.gsf.2022.101520.

Štípská, P., Schulmann, K., Soejono, I., Peřestý, V., Kylander-Clark, A.R.C., Collett, S., Aguilar, C., Maierová, P., Racek, M., Hanžl, P., 2024. Supra-subduction thickening of a continental back-arc: Ediacaran–early Cambrian (Baikalian) metamorphism in the NE Baidrag block (Mongolian Collage). Gondw. Res. 135, 234–265. https://doi.org/10.1016/j.gr.2024.08.007.

Sukhbaatar, T., Lexa, O., Schulmann, K., Aguilar, C., Štípská, P., Wong, J., Jiang, Y., Míková, J., Zhao, D., 2022. Paleozoic geodynamics and architecture of the southern part of the Mongolian Altai Zone. Tectonics 41, e2022TC007498. https://doi.org/10.1029/2022TC007498.

Sukhbaatar, T., Schulmann, K., Janoušek, V., Soejono, I., Lexa, O., Míková, J., Hora, J.M., Song, D., Xiao, W., Poujol, M., Onongoo, T., Dashdorjgochoo, O., Zeng, H., 2024. Magmatic and sedimentological arguments for an Ediacaran active margin in the Bayankhongor Zone in western Mongolia, Central Asian Orogenic Belt. Gondwana Res. 134, 385–409. https://doi.org/10.1016/j.gr.2024.07.017.

Sun, S.S., McDonough, W.F., 1989. Chemical and isotopic systematics of oceanic basalts: Implications for mantle composition and processes. Geol. Soc. Spec. Publ. 42, 313–345. https://doi.org/10.1144/GSL.SP.1989.042.01.19.

Suzaño, N., Becchio, R., Sola, A., Ortiz, A., Nieves, A., Quiroga, M., Fuentes, G., 2017. The role of magma mixing in the evolution of the Early Paleozoic calc-alkaline granitoid suites. Eastern magmatic belt, Puna, NW Argentina. J. S. Am. Earth Sci. 76, 25–46. https://doi.org/10.1016/j.jsames.2017.02.008.

Sylvester, P.J., 1998. Post-collisional strongly peraluminous granites. Lithos 45, 29–44. https://doi.org/10.1016/S0024-4937(98)00024-3.

Tang, J., Xu, W.L., Wang, F., Zhao, S., Wang, W., 2016. Early mesozoic southward subduction history of the Mongol-Okhotsk oceanic plate: evidence from geochronology and geochemistry of Early Mesozoic intrusive rocks in the Erguna Massif, NE China. Gondwana Res. 31, 218–240. https://doi.org/10.1016/j.gr.2014.12.010.

Taylor, S.R., McLennan, S.M., 1985. The Continental Crust: Its Composition and Evolution. https://doi.org/10.1016/0031-9201(86)90093-2.

Thompson, A.B., Schulmann, K., Ježek, J., Tolar, V., 2001. Thermally softened continental extensional zones (arcs and rifts)as precursors to thickened orogenic belts. Tectonophysics 332, 115–141. https://doi.org/10.1016/S0040-1951(00)00252-3.

Tomurtogoo, O., Windley, B.F., Kröner, A., Badarch, G., Liu, D.Y., 2005. Zircon age and occurrence of the Adaatsag ophiolite and Muron shear zone, central Mongolia: Constraints on the evolution of the Mongol-Okhotsk Ocean, suture and orogen. J. Geol. Soc. London 162, 125–134. https://doi.org/10.1144/0016-764903-146.

Uchida, E., Endo, S., Makino, M., 2007. Relationship between solidification depth of granitic rocks and formation of hydrothermal ore deposits. Resour. Geol. 57, 47–56. https://doi.org/10.1111/j.1751-3928.2006.00004.x.

Vernikovskaya, A.E., Vernikovsky, V.A., Sal'nikova, E.B., Datsenko, V.M., Kotov, A.B., Kovach, V.P., Travin, A.V., Yakovleva, S.Z., 2002. Yeruda and Chirimba granitoids (yenisei ridge) as indicators of neoproterozoic collisions. Geol. Geofiz 43, 259–272.

Vernikovskaya, A.E., Vernikovsky, V.A., Sal'nikova, E.B., Kotov, A.B., Kovach, V.P., Travin, A.V., Palesskii, S.V., Yakovleva, S.Z., Yasenev, A.M., Fedoseenko, A.M., 2003. Neoproterozoic postcollisional granitoids of the Glushikha Complex, Yenisei Range. Petrology 11, 48–61.

Vernikovskaya, A.E., Vernikovsky, V.A., Sal'nikova, E.B., Kotov, A.B., Kovach, V.P., Travin, A.V., Wingate, M.T.D., 2007. A-type leucogranite magmatism in the evolution of continental crust on the western margin of the Siberian craton. Russian Geology and Geophysics 48, 3–16. https://doi.org/10.1016/j.rgg.2006.12.002.

Vernikovsky, V.A., Vernikovskaya, A.E., Wingate, M.T.D., Popov, N.V., Kovach, V.P., 2007. The 880-864 Ma granites of the Yenisey Ridge, western Siberian margin: Geochemistry, SHRIMP geochronology, and tectonic implications. Precambr. Res. 154, 175–191. https://doi.org/10.1016/j.precamres.2006.12.006.

Walters, J.B., 2022. MinPlot: a mineral formula recalculation and plotting program for electron probe microanalysis. Mineralogia 53, 51–66. https://doi.org/10.2478/mipo-2022-0005.

Wang, P., Zhao, G., Liu, Q., Han, Y., Yao, J., Li, J., 2020. Zircons from the Tarim basement provide insights into its positions in Columbia and Rodinia supercontinents. Precambr. Res. 341, 105621. https://doi.org/10.1016/j.precamres.2020.105621.

Wang, T., Tong, Y., Xiao, W., Guo, L., Windley, B.F., Donskaya, T., Li, S., Tserendash, N., Zhang, J., 2022. Rollback, scissor-like closure of the Mongol-Okhotsk Ocean and formation of an orocline: magmatic migration based on a large archive of age data. Natl. Sci. Rev. 9, nwab210. https://doi.org/10.1093/nsr/nwab210.

Wang, T., Zheng, Y., Gehrels, G.E., Mu, Z., 2001. Geochronological evidence for existence of south Mongolian microcontinent—A zircon U–Pb age of granitoid gneisses from the Yagan-Onch Hayrhan metamorphic core complex. Chinese Sci. Bull. 45, 2005–2008. https://doi.org/10.1007/BF02901917.

Whalen, J.B., Currie, K.L., Chappell, B.W., 1987. A-type granites: geochemical characteristics, discrimination and petrogenesis. Contrib. Miner. Petrol. 95, 407–419. https://doi.org/10.1007/BF00402202.

White, A.J.R., Chappell, B.W., 1988. Some supracrustal (S-type) granites of the Lachlan Fold Belt. Trans. R. Soc. Edinb. Earth Sci. 79, 169–181. https://doi.org/10.1017/S026359330001419X.

Windley, B.F., Alexeiev, D., Xiao, W., Kröner, A., Badarch, G., 2007. Tectonic models for accretion of the Central Asian Orogenic Belt. J. Geol. Soc. London 164, 31–47. https://doi.org/10.1144/0016-76492006-022.

Wu, F.Y., Liu, X.C., Ji, W.Q., Wang, J.M., Yang, L., 2017. Highly fractionated granites: Recognition and research. Sci. China Earth Sci. 60, 1201–1219. https://doi.org/10.1007/s11430-016-5139-1.

Wu, F.Y., Sun, D.Y., Ge, W.C., Zhang, Y.B., Grant, M.L., Wilde, S.A., Jahn, B.M., 2011. Geochronology of the Phanerozoic granitoids in northeastern China. J. Asian Earth Sci. 41, 1–30. https://doi.org/10.1016/j.jseaes.2010.11.014.

Xiao, W., Windley, B.F., Han, C., Liu, W., Wan, B., Zhang, J., Ao, S., Zhang, Z., Song, D., 2018. Late Paleozoic to early Triassic multiple roll-back and oroclinal bending of the Mongolia collage in Central Asia. Earth Sci. Rev. 186, 94–128. https://doi.org/10.1016/j.earscirev.2017.09.020.

Xiao, W., Windley, B.F., Sun, S., Li, J., Huang, B., Han, C., Yuan, C., Sun, M., Chen, H., 2015. A tale of amalgamation of three Permian-Triassic collage systems in central Asia: Oroclines, sutures, and terminal accretion. Annu. Rev. Earth Planet. Sci. 43, 477–507. https://doi.org/10.1146/annurev-earth-060614-105254.

Xu, Z.Q., He, B.Z., Zhang, C.L., Zhang, J.X., Wang, Z.M., Cai, Z.H., 2013. Tectonic framework and crustal evolution of the Precambrian basement of the Tarim Block in NW China: New geochronological evidence from deep drilling samples. Precambr. Res. 235, 150–162. https://doi.org/10.1016/j.precamres.2013.06.001.

Yakubchuk, A., 2008. Re-deciphering the tectonic jigsaw puzzle of northern Eurasia. J. Asian Earth Sci. 32, 82–101. https://doi.org/10.1016/j.jseaes.2007.10.009.

Yarmolyuk, V., Kovalenko, V., Sal'nikova, E., Kozakov, I., Kotov, A., Kovach, V., Vladykin, N., Yakovleva, S., 2005. U–Pb-Age of sin- and postmetamorphic granitoids from Southern Mongolia - evidence for the presence of grenvilides in the Central Asian Fold Belt. Dokl. Earth Sci. 404, 84–89.

Yarmolyuk, V.V., Kovach, V.P., Kovalenko, V.I., Salnikova, E.B., Kozlovskii, A.M., Kotov, A.B., Yakovleva, S.Z., Fedoseenko, A.M., 2011. Composition, sources, and mechanism of continental crust growth in the Lake Zone of the Central Asian Caledonides: I. geological and geochronological data. Petrology 19, 55–78. https://doi.org/10.1134/S0869591111010085.

Zhao, G., Li, S., Sun, M., Wilde, S.A., 2011. Assembly, accretion, and break-up of the Palaeo-Mesoproterozoic Columbia supercontinent: Record in the North China Craton revisited. Int. Geol. Rev. 53, 1331–1356. https://doi.org/10.1080/00206814.2010.527631.

Zhao, G., Sun, M., Wilde, S.A., Li, S., 2004. A paleo-mesoproterozoic supercontinent: Assembly, growth and breakup. Earth Sci. Rev. 67, 91–123. https://doi.org/10.1016/j.earscirev.2004.02.003.

Zhao, G., Wang, Y., Huang, B., Dong, Y., Li, S., Zhang, G., Yu, S., 2018. Geological reconstructions of the East Asian blocks: from the breakup of Rodinia to the assembly of Pangea. Earth Sci. Rev. 186, 262–286. https://doi.org/10.1016/j.earscirev.2018.10.003.

Zhao, P., Xu, B., Jahn, B.M., 2017. The Mongol-Okhotsk Ocean subduction-related Permian peraluminous granites in northeastern Mongolia: Constraints from zircon U–Pb ages, whole-rock elemental and Sr-Nd-Hf isotopic compositions. J. Asian Earth Sci. 144, 225–242. https://doi.org/10.1016/j.jseaes.2017.03.022.

Zhou, J.B., Wilde, S.A., Zhao, G.C., Han, J., 2018. Nature and assembly of microcontinental blocks within the Paleo-Asian Ocean. Earth Sci. Rev. 186, 76–93. https://doi.org/10.1016/J.EARSCIREV.2017.01.012.

Zhou, L.G., Xia, Q.X., Zheng, Y.F., Chen, R.X., Hu, Z., Yang, Y., 2015. Tectonic evolution from oceanic subduction to continental collision during the closure of Paleotethyan ocean: Geochronological and geochemical constraints from metamorphic rocks in the Hong'an orogen. Gondw. Res. 28, 348–370. https://doi.org/10.1016/j.gr.2014.03.009.

Zhou, T., Liu, Y., Guan, Q., Liu, B., Xiao, W., Li, S., Chen, Z., Peskov, A.Y., 2025. Tectonic evolution of the eastern Central Asian Orogenic Belt during the Carboniferous–Permian. Earth Sci. Rev. https://doi.org/10.1016/j.earscirev.2025.105046.

Zhu, G.Y., Chen, Z.Y., Chen, W.Y., Yan, H.H., Zhang, P.H., 2021. Revisiting to the Neoproterozoic tectonic evolution of the Tarim Block, NW China. Precambrian Res. 352, 106013. https://doi.org/10.1016/j.precamres.2020.106013.

Zhu, M., Pastor-Galán, D., Miao, L., Zhang, F., Ganbat, A., Li, S., Yang, S., Wang, Z., 2023a. Evidence for early Pennsylvanian subduction initiation in the Mongol–Okhotsk Ocean from the Adaatsag ophiolite (Mongolia). Lithos 436–437, 106951. https://doi.org/10.1016/j.lithos.2022.106951.

Zhu, M., Pastor-Galán, D., Smit, M.A., Sanchir, D., Zhang, F., Liu, C., Luo, Y., Miao, L., 2024. The beginning of a wilson cycle in an accretionary orogen: the Mongol–Okhotsk Ocean Opened Assisted by a Devonian Mantle Plume. Geophys. Res. Lett. 51, e2024GL109028. https://doi.org/10.1029/2024GL109028.

Zhu, M., Yan, Z., Pastor-Galán, D., Chen, L., Miao, L., Zhang, F., Li, S., Yang, S., 2023b. Do microcontinents nucleate subduction initiation? Geology 51, 668–672. https://doi.org/10.1130/G51222.1.

Zhu, M., Zhang, F., Miao, L., Baatar, M., Anaad, C., Yang, S., Li, X., 2016. Geochronology and geochemistry of the Triassic bimodal volcanic rocks and coeval A-type granites of the Olzit area, Middle Mongolia: Implications for the tectonic evolution of Mongol-Okhotsk Ocean. J. Asian Earth Sci. 122, 41–57. https://doi.org/10.1016/j.jseaes.2016.03.001.

Zhu, M.S., Zhang, F., Miao, L.C., Baatar, M., Anaad, C., Yang, S.H., Li, X.B., 2018. The late carboniferous Khuhu Davaa ophiolite in northeastern Mongolia: Implications for the tectonic evolution of the Mongol–Okhotsk Ocean. Geol. J. 53, 1263–1278. https://doi.org/10.1002/gj.2955.

Zhu, M., Zhang, F., Miao, L., Ganbat, A., Baatar, M., Anaad, C., Yang, S., Wang, Z., 2023c. Permian–Triassic magmatic rocks in the Middle Gobi volcanic-plutonic belt, Mongolia: revisiting the scissor-like closure model of the Mongol-Okhotsk Ocean. Int. J. Earth Sci. 112, 741–763. https://doi.org/10.1007/s00531-022-02271-5.

Zorin, Y.A., 1999. Geodynamics of the western part of the Mongolia-Okhotsk collisional belt, Trans-Baikal region (Russia) and Mongolia. Tectonophysics 306, 33–56. https://doi.org/10.1016/S0040-1951(99)00042-6.